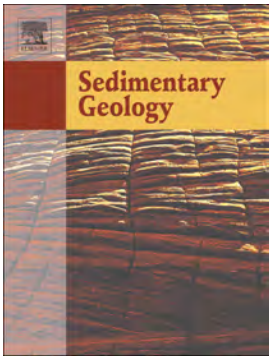

INTRASEDIMENT gypsum in subtidal offshore carbonates as a witness of basin-wide evaporitic precipitation. The CASE of the southern VARISCAN foreland basin (mid-carboniferous)

Iván Díaz-García, Óscar Merino-Tomé, I. Emma Quijada, Juan R. Bahamonde, Luis P. Fernández, Giovanna Della Porta, Elias Samankassou, Elena Kulagina, Ángeles G. Borrego, Jaime Martín-Llaneza, José Federico Del Pozo

PII: S0037-0738(24)00028-9

DOI: https://doi.org/10.1016/j.sedgeo.2024.106605

Reference: SEDGEO 106605

To appear in: *Sedimentary Geology*

Received date: 23 November 2023

Revised date: 11 February 2024

Accepted date: 13 February 2024

Please cite this article as: I. Díaz-García, Ó. Merino-Tomé, I.E. Quijada, et al., INTRASEDIMENT gypsum in subtidal offshore carbonates as a witness of basin-wide evaporitic precipitation. The CASE of the southern VARISCAN foreland basin (mid-carboniferous), *Sedimentary Geology* (2024), https://doi.org/10.1016/j.sedgeo.2024.106605

INTRASEDIMENT GYPSUM IN SUBTIDAL OFFSHORE CARBONATES AS A WITNESS OF BASIN-WIDE EVAPORITIC PRECIPITATION. THE CASE OF THE SOUTHERN VARISCAN FORELAND BASIN (MID-CARBONIFEROUS)

Iván Díaz-García[1]*, Óscar Merino-Tomé[1], I. Emma Quijada[1], Juan R. Bahamonde[1], Luis P. Fernández[1], Giovanna Della Porta[2], Elias Samankassou[3], Elena Kulagina[4], Ángeles G. Borrego[5], Jaime Martín-Llaneza[1], José Federico Del Pozo[1]

[1]Departamento de Geología, Universidad de Oviedo. Oviedo, Spain.

[2]Dipartimento di Scienze della Terra, Università degli Studi di Milano. Milan, Italy.

[3]Département des sciences de la Terre, Université de Genève. Geneva, Switzerland.

[4]Institute of Geology – Subdivision of the Ufa Federal Research Centre of the Russian Academy of Sciences (IG UFRC RAS). Ufa, Russia.

[5]Instituto de Ciencia y Tecnología del Carbono (INCAR-CSIC). Oviedo, Spain.

*Corresponding author: ivan.diazgarc@gmail.com

Abstract

Widespread calcite and quartz pseudomorphs, interpreted as originally gypsum crystals, occur within calci-mudstone accumulated in subtidal offshore environments in the broad marine foreland basin developed on the southern flank of the Ouachita–Alleghanian–Variscan Orogen during mid-

Carboniferous times, which acted as a marine corridor connecting the Panthalassa and Palaeo-Tethys Oceans during the Mississippian, and progressively narrowed during the assembly of Pangea. In this study, 67 outcrops of radiolaria-bearing calci-mudstone deposits that contain calcite and quartz pseudomorphs located in northern Spain and southern France were studied to constrain the gypsum spatial distribution and sedimentological features. The recognized microfacies indicate intrasediment gypsum precipitation, accompanied by less abundant bottom-grown precipitates and gypsum cumulates, in extensive subtidal offshore (sublittoral below wave base to bathyal) environments. Gypsum precipitation took place during a short-lived temporal episode during the early Bashkirian time (Voznesenkian), which can be correlated, on the basis of benthic foraminifera, with the coastal (inter- to supratidal) gypsum evaporites identified in NW Africa (Tindouf and Reggan successions in Morocco and Algeria) that would represent the shallow-water counterparts. The occurrence of gypsum precipitates both in subtidal offshore calci-mudstones of the Variscan foreland basin and in inter- to supratidal environments of the Sahara epeiric shelf indicate that hypersaline conditions affected vast marine areas, roughly coinciding with the estimated age of closure of the Panthalassa and Palaeo-Tethys marine connection. Therefore, the studied succession represents the trace of a basin-wide evaporitic episode extending for hundreds of kilometres driven by foreland basin restriction, mid-Carboniferous sea-level fall and arid climate. This study provides new insights for the interpretation of gypsum precipitates in subtidal offshore marine environments encountered in the Phanerozoic and whose genesis is poorly understood.

Keywords: Marine evaporites, intrasediment gypsum, Carboniferous, Variscan foreland basin, Barcaliente Fm

1. INTRODUCTION

Evaporites are commonly recognized in coastal and shallow-marine (littoral) sedimentary successions (Warren and Kendall, 1985; Demicco and Hardie, 1994; Ortí, 2010a; Warren, 2016). However, they can also occur in deep-water settings when hypersaline conditions (i.e. higher than normal marine, Ortí, 2010a) extend across restricted marine basins. The best-known examples are the Permian Zechstein Basin and the Mediterranean Basin during the Messinian salinity crisis (e.g. Schlager and Bolz, 1977; Tucker, 1991; Lugli et al., 2015; Warren, 2016; Manzi et al., 2021). Evaporite cumulates and reworked clastic evaporites are described in the literature as typical features of deep-marine deposits (Bąbel 1999; 2004; Lugli et al., 2015; Warren, 2016; Ben Dor et al., 2019). In contrast, displacive evaporites, which are typical of shallow (littoral) environments such as supratidal sabkhas (Bąbel, 2004; Warren, 2016), have been rarely described in deep-marine deposits (Lugli et al., 2015; Natalicchio et al., 2021). Although the study of modern sabkhas and playa-lakes has helped to decipher the factors leading to intrasediment evaporite precipitation in shallow environments (Purser and Evans, 1973; Warren, 2016), the lack of modern analogues for marine evaporite basins limits the understanding of intrasediment evaporite precipitates in deep-water environments.

Here we report the widespread occurrence of calcite and quartz pseudomorphs after intrasediment gypsum crystals in a subtidal offshore calci-mudstone succession as thick as 30 metres accumulated in the foreland basin developed on the southern flank of the Ouachita-Alleghanian-Variscan Orogen during mid-Carboniferous times (Fig. 1). The studied deposits accumulated over an area of 192,000-231,000 km^2 (>770 km in length and 250-300 km in width according to a palinspastic restoration after the present-day distribution of the strata studied in northern Spain and southern France). This study aims at exploring the origin of gypsum crystals, their mode of precipitation and depositional environment, and the mechanisms that led to gypsum precipitation in the marine foreland basin. The genesis of the associated carbonate mud is out of the scope of the study. Considering that these strata with calcite and quartz pseudomorphs after gypsum constitute one of the rare examples in which intrasediment gypsum crystals are recognized in subtidal offshore calci-mudstone deposits, this study provides a better understanding of the mechanisms involved in the precipitation of intrasediment gypsum in deep-water environments. Furthermore, this study provides new information on the palaeogeographic and palaeoclimatic evolution of the equatorial zone of Pangea during the Laurentia–Gondwana collision in the mid-Carboniferous.

2. GEOLOGICAL SETTING

The marine foreland basin developed south of the Ouachita–Alleghanian–Variscan orogen acted as a corridor between Panthalassa and

Palaeo-Tethys Oceans during Mississippian times (Fig. 1A). This basin was progressively restricted due to tectonic convergence of Gondwana and Laurussia and eventually closed around the Mississippian–Pennsylvanian boundary (Blakey, 2008; Davydov and Cózar, 2019). The distalmost sectors of this basin connected southwards with the vast epeiric marine shelf developed north of Gondwana (the Sahara Platform).

The studied deposits form part of the Carboniferous succession that crops out along the foreland fold and thrust belt of the Variscan Orogen at the core of the Ibero-Armorican Arc (Fig. 1B): the so-called Cantabrian Zone (CZ, onwards) of the Iberian Variscan Massif (Lotze, 1945), and in the Axial Zone of the Pyrenees in northern Spain and southern France (Pyrenees, onwards). The Carboniferous succession consists of 15–40 m-thick pelagic condensed red-nodular limestones, radiolarites and black laminated calci-mudstones, red shales and marlstones (Alba Fm in the CZ and Aspe Brousset Fm in the Pyrenees; Fig. 2), and 60–400 m-thick dark grey and laminated calci-mudstone with radiolaria (Barcaliente Fm in the CZ, and Iraty Fm and Aranza and Chourique Lmst. in the Pyrenees), which accumulated over broad areas of the basin during Visean to early Bashkirian times (Figs. 1B and 2) (see Colmenero et al., 2002; Fernández et al., 2004; Merino-Tomé et al., 2019; Sanz-López et al., 2019). Towards the basin foredeep, these successions pass laterally into deep-water siliciclastic turbidites (Olleros Fm in the CZ and Culm Group in the Pyrenees; Fig. 2). These deposits are overlain by the Bashkirian–Moscovian microbial carbonate platforms recognized in the CZ by numerous authors (see Eichmüller, 1985, 1986; Della Porta et al., 2003; Kenter et al., 2003; Bahamonde et al., 2007, 2015, 2017; Chesnel et al., 2016) (Fig. 2).

More specifically, this study focuses on a metre- to decametre-thick interval in the upper part of the Barcaliente Fm and its equivalent stratigraphic units in the Pyrenees that contain calcite and quartz pseudomorphs after gypsum (Figs. 3 and 4). Previous authors have locally reported the presence of these pseudomorphs in the CZ and interpreted them as being originally gypsum crystals (González Lastra, 1978; Sánchez de la Torre and González Lastra, 1978; Sánchez de la Torre et al., 1983), whereas some others interpreted them as formerly authigenic quartz crystals (Winkler Prins, 1971; Hemleben and Reüther, 1980). In the CZ, this stratigraphic interval is overlain in numerous localities by a 6–85 m-thick carbonate breccia, named Porma Breccia (Reuther, 1977). Although this stratigraphic interval was traditionally interpreted as recording evaporite deposition in restricted inter- to supratidal settings (González Lastra, 1978; Sánchez de la Torre and González Lastra, 1978; Sánchez de la Torre et al., 1983; Eichmüller, 1985, 1986), this interpretation is reviewed here in the light of the new sedimentologic data acquired in this research.

3. METHODS

3.1. Fieldwork

Fieldwork was designed to provide data on mid-Carboniferous strata with calcite and quartz pseudomorphs to constrain their spatial distribution, describe their stratigraphy and facies, and accurately define their age. These deposits and associated carbonate breccias were observed in 64 localities of the

CZ (Fig. 1B and 3A) plus 3 other localities in the central and western part of the Variscan exposures in the Axial zone of the Pyrenees (Aragón Subordán Valley and Canfranc in Spain, and Aspe-Brousset Valley in France; Fig. 1B). A detailed characterization of the strata with calcite and quartz pseudomorphs including the description of stratigraphic logs at a decimetre scale, acquisition of sedimentologic information and rock sampling for further petrographic studies (including microfacies analysis), was carried out in 23 of the above-mentioned outcrops (21 in the CZ and two in the Pyrenees). This data set was complemented with precise measurements of the total thickness of the strata with calcite and quartz pseudomorphs, facies descriptions and sampling from 25 additional outcrops in the CZ and one in the Pyrenees.

3.2. Petrography and image analysis

Rock samples were cut to obtain polished rock slabs and thin sections for macroscopic observations and facies characterization. More than 525 thin sections were studied for microfacies analysis using a polarised light-transmitted microscope Nikon Eclipse LV100POL equipped with a Nikon DS-Ri2 camera and the image analysis software NIS Elements v.5.10. Visual estimates of the abundance (% per area) of calcite and quartz pseudomorphs, sediment matrix (carbonate mud recrystallized in microsparite–sparite) and bioclasts were made, as well as measurements of the size (Feret diameter, D_F) of the pseudomorphs replacing precursor gypsum.

Point and area counting methodologies (Heilbronner and Barret, 2014) were applied for quantification of the abundance and size of the calcite and quartz pseudomorphs. These image analyses were performed on 65 thin sections scanned with a pixel density ranging from 4000 to 4800 ppi, using open-source software FIJI-ImageJ (Ferreira and Rasband, 2012). Feret diameter (D_F; also called b axis or caliper), area equivalent diameter (D_E), crystal size distribution (CSD) and abundance (% per area) of the pseudomorphs were analysed in 40 of these samples in which the differentiation of many individual crystals was suitable. In further 25 samples, the objective identification and contouring of individual pseudomorphs was not possible due to the common presence of pseudomorph aggregates, and therefore point counting was performed using a grid size of 0.45 mm to obtain accurate information on the calcite pseudomorph abundance.

Optical cathodoluminescence was performed in a total of 49 samples selected from four of the studied sections using an ERI-MRTech equipment coupled with an Olympus BX41 petrographic microscope and using a MK 5-2 luminoscope by Cambridge Image Technology Ltd. (beam voltage of 10 to 16 kV; beam current of 200 to 600 µA; vacuum gauge of 50 to 70 millitor).

SEM petrography was carried out on 13 selected samples of carbonate breccias that included a groundmass replaced by quartz and calcite with solid inclusions. SEM analyses were performed using a scanning electronic microscope JEOL-6610LV with a coupled Energy dispersive X-ray (EDS) analyser INCA Energy 350 - Xmax 50 (energy resolution of 0,125-5,9 keV) and a JEOL-JSM7001F equipped with an EDS detector (model JEOL EX-94300S4L1Q) coupled with a JED 2300 software (energy resolution of 15 kV, probe current of approximately 3.5 nA). More than 115 qualitative compositional analyses of the solid inclusions contained in the quartz and calcite replacements, complemented with 19 local semiquantitative chemical analyses with the EDS detector, provided new insights on the mineralogy of the original groundmass of the breccias.

4. RESULTS

4.1. Stratigraphy of the deposits with calcite and quartz pseudomorphs

The study of the discrete stratal package with calcite and quartz pseudomorphs in the upper part of the Barcaliente Fm and its equivalent stratigraphic units from the Pyrenees shows that it has an almost widespread distribution across both the CZ and Pyrenees (see Figs. 3 and 4). Locally, scarce pseudomorphs were identified in older strata (VV section, Fig. 3B).

The total current thickness of the stratigraphic package bearing calcite and quartz pseudomorphs ranges from 4 m (INT section; supplementary data) to 30 m (HV section; see Fig. 3B and 4). Along the studied outcrops the base of the pseudomorph-bearing strata generally corresponds to a gradual transition with underlying dark-grey laminated radiolarian calci-mudstones. In general terms, from the base towards the top of the interval there is a progressive increase in pseudomorph abundance accompanied by a gradual reduction of the pseudomorph size and a change in their arrangement, from scattered to arranged into laminae (Fig. 4; P section). In the outcrops closest to the foredeep (Fig. 4; R and VV section), calcite pseudomorphs are recognized in sandstone and intraclastic rud- to packstone strata interbedded with calcareous debris-flow deposits or laminated radiolarian calci-mudstones, marlstone and shales.

The stratigraphic interval bearing calcite and quartz pseudomorphs of the upper part of the Barcaliente Fm and equivalent stratigraphic units is overlain either by dark-grey radiolarian-rich wackestones, or light-grey bioclastic limestones and common microbial boundstone strata of the Valdeteja Fm (Fig. 2, 3B and 4). The transition to these deposits shows variable features:

- In broad areas of the CZ, a breccia unit appears atop of the strata with calcite and quartz pseudomorphs, which has been informally named Porma Breccia (Reuther, 1977). This breccia unit is locally up to 85 m thick and is composed of fragments of calci-mudstone with calcite and quartz pseudomorphs and, towards its upper part, it contains also fragments of the overlying strata (generally dark-grey radiolarian wackestone and locally microbial boundstone; Fig. 4). Comparable breccias have also been observed in some of the studied sections in the Pyrenees (CH section).
- In certain specific areas, the top of the strata with calcite and quartz pseudomorphs consists of an irregular surface overlain by yellowish to ochre nodular breccias (CL section; Fig. 4).
- In scattered locations, the contact between the strata bearing calcite and quartz pseudomorphs and the overlying dark grey radiolarian wackestones is a normal contact with no erosional features and no brecciation (VV, and MA sections; Fig. 4).

The studied stratal package with calcite and quartz pseudomorphs lies above the First Appearance Datum (FAD) of the conodont *Declinognathodus inaequalis* and *Idiognathoides corrugatus* (Sanz-López et al., 2013). Samples collected in this study from strata overlying the aforementioned stratal package in the CQ section show foraminifera associations that are typical for uppermost Serpukhovian–lowermost Bashkirian (Voznesenkian–Krasnopolyanian) strata. Ordinary species are *Endothyra* ex gr. *bowmani* (Phillips, 1846), *Bradyina cribrostomata* (Rauser-Chernousova and Reitlinger in Rauser-Chernousova, 1937), *Eostaffella statuta* (Reitlinger, 1980), *Eostaffella acutiformis* (Kireeva in Rauser-Chernousova et al., 1951), *Ikensieformis* cf. *mirifica* (Brazhnikova in Brazhnikova et al., 1967), *Ikensieformis postproikensis* (Vdovenko in Brazhnikova et al., 1967), Asteroarchaediscidae, *Howchinia bradyana* (Howchin, 1888 = *Howchinia gibba longa*, Brazhnikova in Brazhnikova et al., 1967), *Monotaxinoides transitorius* (Brazhnikova and Jartzeva, 1956), and *Janischewskina* sp. (Fig. 5). In the case of the HV section, samples collected from strata lying 23 m above the studied stratal package provided a foraminiferal association characterized by abundant archaediscids and eostaffellids with scarce representatives of the *Plectostaffella* genera consisting of: *Monotaxinoides* cf. *transitorius* (Brazhnikova and Jartzeva, 1956), *Neoarchaediscus* cf. *postrugosus* (Reitlinger, 1949), *Asteroarchaediscus bashkiricus* (Krestovnikov and Theodorovich, 1936), *Eostaffella postmosquensis* (Kireeva in Rauser-Chernousova et al., 1951), *Parastaffella* sp., *Plectostaffella* ex gr. *Varvariensis* (Brazhnikova and Potievska, 1948) (Fig. 6).

4.2. Facies

Three main groups of facies have been recognized within the stratigraphic package bearing calcite and quartz pseudomorphs within the Barcaliente Fm and its equivalent stratigraphic units: 1) facies devoid of calcite and quartz pseudomorphs (facies A and B); 2) facies with calcite and quartz pseudomorphs (facies C, D, E, F and G); and 3) carbonate breccias with clasts deriving from fractured or reworked/altered strata belonging to facies listed above under 1 and 2 (facies H and I).

4.2.1. Facies A. Dark-grey calci-mudstones to wackestones with scarce radiolaria

It is the dominant facies in the Barcaliente and Iraty Fms and in the Aranza and Chourique Lmst, and consists of centimetre to decimetre-thick tabular to wavy beds. This facies also occurs interbedded with the facies bearing calcite and quartz pseudomorphs (facies C, D, E, F, G) and overlying the stratigraphic interval with calcite and quartz pseudomorphs (Fig. 4). It consists of calci-mudstones with a variable percentage of very small peloids (generally <10 μm in diameter). Carbonate mud forming the sediment matrix is recrystallized into microsparite and sparite (Fig. 7A). The most common bioclasts correspond to spherical calcitized (and less commonly pyritized) radiolaria (Fig. 7A, B) and very scarce ostracods. In addition, previous authors have also reported very scarce heterotrophic benthic fauna in this facies, including crinoid and holothurian plates, sponge spicules, brachiopods, and very scarce conodonts, calcispheres and agglutinated foraminifera (Eichmüller, 1985, 1986; Sanz-López and Blanco-Ferrera, 2013; Sanz-López et al., 2013). Although this facies is slightly bioturbated, sub-millimetre-size horizontal lamination is commonly recognized.

Interpretation

The carbonate mud-dominated texture with parallel lamination that characterizes facies A together with the absence of coarse silt- to sand-grade sediment, of erosional surfaces veneered with coarse (bioclastic) lags, and of tractional deposits (Dott and Bourgeois, 1982; Clifton, 1988; Son et al., 2012; amongst others), suggest sedimentation in a subtidal offshore (i.e. below the wave base) setting. A similar interpretation was also given by Nemyrovska et al. (2011) for the equivalent facies of the Barcaliente Fm in the Lastra section (SE of the study area, Palentian Zone, Cantabrian Mountains, see Fig. 3 for location). Furthermore, the low degree of bioturbation and the reported skeletal associations (dominated by radiolaria and ostracods, and characterized by the scarcity of shallow-water benthic biota and, in particular, of benthic photozoans) are compatible with subtidal offshore environments, and might also suggest prevailing dysphotic to aphotic conditions (cf. Flügel, 2010). In fact, the recorded conodont associations are characteristic of deep-water conodont zonation for Northern Spain and Eurasia (Barrick, 2021).

4.2.2. Facies B. Dark-grey radiolarian wackestones

This facies occurs in limestone beds overlying the stratal package with calcite and quartz pseudomorphs (Fig. 4). It consists of centimetre to decimetre-thick tabular to wavy beds with marly interbeds and is composed of burrowed to laminated radiolarian-rich wackestones with a variable percentage of other bioclasts, including small foraminifera (tuberitinids, lasiodiscids, calcivertellids, endothyrids and archaediscids), ostracods, siliceous sponge spicules, brachiopods, crinoids, trilobite fragments and scattered ammonoids (Fig. 7C, D). Carbonate mud forming the rock matrix is generally recrystallized into microsparite and rarely into sparite. Although bioturbation is ubiquitous in facies B, some laminated intervals are also present. Silica replacement of both sediment matrix and skeletal grains (Fig. 6) is a common diagenetic feature and millimetre to centimetre-sized chert nodules can be observed in the field. Sediment distortion and fluid escape-like structures can be commonly recognized.

Interpretation

As with facies A, the carbonate-mud-dominated texture, occasionally with parallel lamination, which characterizes facies B is indicative of deposition in a low-energy subtidal offshore setting. However, the low grade of preservation of lamination due to abundant bioturbation and the presence of common bioclasts reflect higher biological activity compared to facies A and to facies containing calcite and quartz pseudomorphs present in the underlying stratigraphic interval. Eichmüller (1986), Della Porta et al. (2003) and Chesnel et al., (2016) recorded this facies as one of the typical basin deposits accumulated adjacent to the Bashkirian high-relief carbonate platforms of Valdeteja, Sierra del Cuera and Valdorria, respectively.

4.2.3. Facies C. Calci-mudstones with scattered calcite and quartz pseudomorphs after intrasediment gypsum

Together with facies D, this is the most abundant and widespread facies in the studied stratigraphic interval and shows an almost ubiquitous distribution throughout the measured outcrops of the basin. Facies C is the dominant facies in the lower part of the pseudomorph-bearing package studied and shows gradual vertical transitions to both the underlying strata devoid of pseudomorphs (facies A) and the overlying calci-mudstones with laminae of calcite and quartz pseudomorphs after intrasediment gypsum (facies D).

Facies C consists of calci-mudstones characterized by the presence of predominantly calcite and quartz pseudomorphs (Fig. 8A). Calci-mudstone beds consist of microsparite and show a sub-millimetre-thick lamination that generally mimics the shapes of the pseudomorphs (Fig. 8B, C). They contain rare radiolarian biomoulds and ostracods. The pseudomorphs show monoclinic prismatic and equant hexagonal morphologies and, less frequently, lenticular shapes (Fig. 8A, B, C). The b-axes of the pseudomorphs are generally greater than 1 mm with maximum values of 5 mm in most samples, although they can reach centimetre sizes in some beds (Fig. 8A). Image analyses show an average D_E of evaporite crystals of 615–908 µm (Fig. 9A, B) and a wide range of CSD; D_F mean values are 816–1246 µm. The abundance of calcite pseudomorphs after evaporites in this facies is usually below 20% per area (Fig. 9C). In samples with larger and more abundant pseudomorphs, the pseudomorphs cluster to form millimetre- to centimetre-sized aggregates. Although calcite and quartz replacements of pseudomorphs are the most abundant (Fig. 8A), replacements by celestite, dolomite, pyrite and fluorite have also been observed locally.

Interpretation

The monoclinic, equant hexagonal and lenticular habits of the pseudomorphs are characteristic of gypsum crystals (e.g. Palache et al., 1951; Ortí et al. 1984, 2014; Magee, 1991; Kendall, 1992; Paik et al., 2007; Ortí, 2010a; Quijada et al., 2013; Natalicchio et al., 2021; Reiss et al., 2021).. The abundance of carbonate mud around the pseudomorphs after gypsum crystals and the random crystal orientations (Figs. 8A-C) are indicative of intrasediment gypsum precipitation, which occurred at, or slightly underneath, the sediment–water interface. Similar intrasediment gypsum crystals precipitate interstitially in microbial mats of present-day marine saltworks at salinities of around 140-150‰ (Ortí et al., 1984; Bąbel, 2004; Ortí, 2010b, 2011). The deformation of the sediment lamination around the pseudomorphs may have been the result of displacive gypsum growth (Paik et al., 2007; Ortí, 2010a; Quijada et al., 2013) and/or differential compaction during burial.

Previous studies in the CZ also interpreted the pseudomorphs described in facies C as originally evaporative gypsum crystals (González Lastra, 1978; Sánchez de la Torre and González Lastra, 1978), but precipitated in salina and sabkha settings. However, the fact that the composition of the sediment matrix surrounding the pseudomorphs after gypsum is equivalent to that forming facies A allows inferring that evaporite precipitation took place in low-energy subtidal offshore environments, instead of peritidal environments as proposed by González Lastra, (1978) and Sánchez de la Torre and González Lastra (1978).

4.2.4. Facies D. Calci-mudstones with laminae of calcite and quartz pseudomorphs after intrasediment gypsum

Facies D is composed of laminated calci-mudstones alternating with laminae of aggregates of calcite and quartz pseudomorphs. The sediment matrix shows the same characteristics as those described in facies C, with rare ostracods and very rare radiolarian biomoulds, and a thin lamination that fits the morphology of the evaporite pseudomorph aggregates (Fig. 8D). Laminae of pseudomorphs are laterally continuous over several centimetres to decimetres and range in thickness from hundreds of μm to 2 mm (Fig. 8D). As in facies C, individual crystals of calcite pseudomorphs show mostly monoclinic prismatic and equant hexagonal habits and rare lenticular shapes. Crystal size is generally smaller than in facies C. D_F is commonly less than 600 μm (546–568 μm) and D_E values range from 286 to 413 μm; CSDs exhibit narrower distributions with modal values defining higher peaks than in the case of facies C (Fig. 9A, B). Pseudomorph abundance commonly varies from 20 to 60% per area, reaching more than 60% in some samples (Fig. 9C).

Interpretation

As with facies C, the characteristics of the pseudomorphs and sediment matrix of facies D suggest that this facies was deposited in low-energy subtidal offshore environments. The abundance of carbonate matrix around the pseudomorphs after gypsum crystals and the random crystal orientations (Fig. 8D) are also indicative of intrasediment gypsum precipitation. Nevertheless, the smaller crystal size of intrasediment gypsum and the greater evaporite abundance in facies D than in facies C suggest higher salinities of the brines than in C (cf. Alimi and Gadri, 2004; Reiss et al., 2021). Although several authors have described facies C in the CZ (González Lastra, 1978; Sánchez de la Torre and González Lastra, 1978), facies D has not been previously identified. However, Hemleben and Reüther (1980) reported laminated facies in one of the sections in which facies D was identified in this study (CAB section). These authors interpreted the laminated deposits at this locality as stromatolites instead of ascribing them to an evaporitic origin, probably due to the slightly undulated character of pseudomorph-rich laminae.

4.2.5. Facies E. Calci-mudstones with calcite pseudomorphs after gypsum cumulates

Facies E occurs mostly in association with facies C and, locally, with facies F and G, although its abundance is lower. This facies has been recognised in numerous sections in both the CZ and the Pyrenees, mainly in the upper part of the studied stratigraphic interval. It consists of dark grey calci-mudstones, currently recrystallized in microsparite or sparite, with millimetre- to centimetre-thick laminae composed of relatively well-sorted calcite pseudomorphs with b axis smaller than 50 μm (Fig. 10). The pseudomorph laminae that characterize this facies show a gradual lower contact and a progressive upward increase in pseudomorph abundance (up to 35 to 80%). The upper contact of some pseudomorph laminae is sharp and corresponds to primary crystal terminations (Fig. 10A).

Interpretation

The extremely well-sorted tiny pseudomorphs defining millimetre-thick cycles of increasing abundance of pseudomorphs characterising facies E could correspond to cumulates formed as the result of gypsum crystallization at the brine-air interface or within the water column (particularly at the pycnocline/halocline), with later sinking and accumulation on the basin floor (cf. Castile Fm, Schmalz, 1969; Leslie et al. 1996; Kirkland et al., 2000; Nida Gypsum deposits, Bąbel 1999; Las Minas Gypsum unit, Ortí et al., 2014; Messinian deposits from the Mediterranean Sea, Lugli et al., 2015). The sharp upper contacts showing primary crystal terminations observed in some pseudomorph laminae could have formed by subsequent overgrowth of the cumulate crystals settled in the sediment bottom. Despite their smaller size, the pseudomorphs showing crystal terminations are similar to bottom-grown gypsum described in the Castile Fm (Texas and New Mexico, USA) by Leslie et al. (1996) and in Messinian deposits below the Mediterranean seafloor by Lugli et al. (2015). Observations on present-day marine saltworks show that salinities of 150-230‰ are necessary to precipitate gypsum cumulates and millimetre-sized bottom-grown gypsum crystals (Ortí et al., 1984; Bąbel, 2004; Ortí, 2010b, 2011). The laminated microsparite hosting these gypsum cumulates, similar to the previous facies, also points to deposition in a low-energy subtidal offshore environment, .

4.2.6. Facies F. Microbial carbonates with scattered calcite and quartz pseudomorphs after gypsum

This facies was recognized only in two sectors of the CZ: the distalmost sector (section MA) and the intermediate sector (sections HV, A, Y, CQ and G) of the basin transect shown in Figures 3 and 4. It is common in the upper portion of the studied stratigraphic interval that contains calcite and quartz pseudomorphs.

Facies F consists of homogeneous to clotted micritic to microsparitic laminae with abundant, irregular, submillimetre to millimetre-sized pores filled by blocky calcite cements and, commonly, with calcite and quartz pseudomorphs, which may occur scattered or in laterally continuous laminae. The fabrics of the carbonate sediment together with differences in the morphology and arrangement of the pseudomorphs allow differentiating two subfacies:

- Subfacies F1. Micritic limestone with crinkly to wavy lamination (Fig. 11A) produced by alternating submillimetre- to millimetre-thick, dark micrite (locally clotted) to microsparite laminae and light microsparite–sparite laminae (Fig. 11A, B), or by the presence of small, elongated pores arranged approximately parallel to lamination and filled with blocky calcite (Fig. 11C, D). Locally, this lamination defines positive reliefs with domal geometries up to few centimetres in height and several centimetres to decimetres in width. Radiolarian biomoulds can be abundant and locally represent up to 8% of the sample. Submillimetre to millimetre-sized (b axis), calcite and quartz pseudomorphs with euhedral habits (monoclinic prismatic, equant hexagonal and lenticular habits) are scattered in variable proportions, but lenticular habits and caliper as large as 1–2 cm have also been recognized exceptionally (Fig. 11C).

- Subfacies F2. Slightly wavy laminated limestone composed of dark grey micrite to microsparite with rare to very rare radiolarian biomoulds (<0.1%), interbedded with laminae of aggregates of calcite pseudomorphs after hexagonal equant crystals (Fig. 11E and F). The pseudomorph laminae show lateral continuities of up to several centimetres and thicknesses ranging from hundreds of μm to 3 mm (exceptionally, up to 10 mm), the thicker laminae correspond to those formed by larger the pseudomorphs. The bases of the laminae of pseudomorph aggregates are poorly defined, while the tops generally show sharp contacts corresponding to the original crystal terminations (Fig. 11E). The pseudomorphs are draped by micrite to microsparite in which filamentous structures (Fig. 11F) can be locally recognized. The abundance of calcite and quartz pseudomorphs after gypsum in subfacies F2 is 12 to 27%.

Interpretation

The textures and microstructures reported in facies F (crinkly to wavy lamination, elongated pores parallel to lamination, clotted textures, filamentous structures) are comparable to the textures and microstructures described by many authors in microbial carbonate deposits (e.g. Aitken, 1967; Riding, 2000, 2008; Della Porta et al. 2003; Dupraz et al., 2004; Spadafora et al., 2010; Bahamonde et al. 2017; Suarez-Gonzalez et al., 2019b), which suggest a probable microbial origin for the carbonate sediment of this facies. Observed filamentous structures resembling microbial filaments (e.g. Monty, 1967; Riding, 2000; Pratt, 2001; Suarez-Gonzalez et al., 2019b; Quijada et al., 2020) reinforce this interpretation. Subfacies F1 shows calcite pseudomorphs with similar features to those described in facies C and D, which are interpreted as intrasediment gypsum crystals. However, the characteristics of the aggregates of pseudomorphs observed in subfacies F2 (poorly defined bases and sharp tops showing primary gypsum crystal terminations) could correspond to bottom-grown gypsum precipitates. The co-occurrence of microbialite deposits and intrasediment and/or bottom-grown gypsum is common in present-day and ancient shallow evaporite environments (Ortí et al., 1984; Rouchy and Monty, 2000; Gerdes et al., 2000; Rouchy et al., 2001; Bąbel, 2004), such as Santa Pola salt work (eastern Spain; Ortí et al., 1984), the Trucial Coast (United Arab Emirates, Persian Gulf; Alsharhan and Kendall, 2003; Bontognali et al., 2010), Al Kharrar supratidal–intertidal sabkha (Red Sea coast, Saudi Arabia; Aref and Taj, 2018) and Messinian shallow-marine restricted environments of Mallorca (W Mediterranean; Suarez-Gonzalez et al., 2019a). However, during Carboniferous times microbial deposits formed in a wide range of paleowater depths, including relatively deep subtidal environments, particularly in the CZ (see for example Della Porta et al., 2003; Bahamonde et al., 2007). Thus, in the absence of additional criteria, it is not possible to determine the water depth at which this facies formed.

4.2.7. Facies G. Arenites with calcite pseudomorphs after detrital gypsum

Facies G consists of tabular to wavy, a few centimetre-thick beds, interlayered with facies A and C (Fig. 11A) and marlstone/shales in sections located near the foredeep of the basin (sections R and VV; Fig. 4). Beds show sharp bases, locally displaying erosional features, and sharp to gradational tops below an overlying marlstone/shale division. Internally, they commonly show normal grading, parallel lamination and/or ripple cross-lamination (Fig. 12A and B).

Some arenite beds are composed of well-sorted sand-sized grains of quartz and calcite pseudomorphs, with a relatively low percentage of bioclasts and calcareous intraclasts, and contain mica flakes and tourmaline and zircon grains (Fig. 12C). Other arenite beds consist of sand-sized calcareous grains (mostly bioclasts, coated grains, peloids, and intraclasts), calcite pseudomorphs and scarce terrigenous components (Fig. 12D and E). The calcite pseudomorphs show abraded, monoclinic prismatic and lenticular morphologies. They are homogeneous in size (Fig. 12C, D and E), and their b axis is commonly oriented parallel to lamination. Calcite pseudomorph abundance can reach up to 35%.

Interpretation

Facies G resembles deposits accumulated by diluted gravity flows such as turbidity currents *sensu* Mulder and Alexander (2001). The fact that the pseudomorphs after gypsum are well sorted, commonly oriented parallel to lamination, and display abraded monoclinic and lenticular morphologies, suggests that they were originally detrital gypsum grains (cf. Hardie and Eugster, 1971; Rouchy et al., 1995; Sanz-Montero and Rodríguez-Aranda, 2022). Furthermore, the low abrasion of evaporite crystals would indicate limited transport from adjacent locations (see Lugli et al., 2010).

4.2.8. Facies H. Carbonate breccia with angular–subangular fragments of limestone bearing calcite and quartz pseudomorphs

This facies forms irregular or strata-bound rock bodies interbedded with, cross-cutting or overlying stratigraphic intervals with abundant calcite and quartz pseudomorphs after gypsum (facies C, D, E and F; Fig. 4). The thickness of the breccia bodies ranges from a few centimetres to tens of metres, whereas their lateral extent (from decimetres to kilometres) usually exceeds the size of the studied outcrops. Contacts with the surrounding limestone strata can be gradual or sharp.

The carbonate breccia consists of millimetre- to metre-sized angular fragments of facies A, B, C, D, E, F and G (Fig. 13A and B). The breccia fragments have rectangular prismatic to rhombohedral shapes. Although in many cases fragments show random orientations, they are locally arranged into centimetre- to metre-scale folds (Fig. 13A). In addition, where the contact between the breccia and the adjacent strata is gradual, the original bedding can be preserved and the breccia shows a jigsaw-fit texture.

The groundmass is composed of submillimetre-sized fragments of microsparitic limestone, cloudy spar, and minor quartz and celestite (Fig. 13B and C). Micrometre-sized solid inclusions (caliper of 2–35.5 μm, most frequent sizes of 6.5–9.7 μm) are preserved in both calcite and quartz crystals (Fig. 13D and E).

These inclusions show birefringence colours in crossed polarizers specific of anhydrite (Fig. 13E), and SEM-EDS analyses confirmed that they are composed of calcium sulphate (Fig. 13D).

Interpretation

Facies H is interpreted as the result of brecciation of facies A, B, C, D, E and F. The fact that these breccias occur within, or atop, stratigraphic intervals characterized by the presence of abundant pseudomorphs after gypsum, as well as their strata-bound geometry, suggest that their formation was closely related to an original large quantity of calcium sulphate in the brecciated layers. Moreover, the prismatic morphologies of the fragments, the gradual contacts with adjacent strata that some of the breccias show and the preservation of the original bedding of the brecciated layers forming a jigsaw-fit texture suggest *in situ* brecciation during burial.

The presence of anhydrite inclusions in the breccia groundmass indicates that the groundmass consisted largely of anhydrite, which probably formed by conversion of the synsedimentary gypsum accumulated in this stratigraphic interval into anhydrite during burial. After the formation of the breccia, the anhydrite was replaced by spar and, to a minor extent, by quartz and celestite. In addition, the groundmass also contains submillimetre-sized fragments of microsparitic limestone, which were probably formed by comminution of the carbonate of facies A, B, C, D, E and F.

The arrangement of breccia fragments into folds observed locally suggests that the brecciation mechanism produced, at least occasionally, a plastic deformation of the anhydrite in the brecciated interval, which might have flowed readily under stress (Müller and Briegel, 1978; Müller et al., 1981; Jordan and Nüesch, 1989; Schreiber and Helman, 2005). The interbedded limestone layers, which have a different rheological behaviour, were broken and rotated.

All these features suggest that the carbonate breccias of facies H were formed during or after sediment burial and lithification. The mechanism triggering brecciation could be related to halokinetic processes, tectonically-induced sulphate flow processes (see Quijada et al., 2014) or hydraulic fracturing (Hurst and Cartwright, 2007).

4.2.9. Facies I. Nodular breccia

This facies (Fig. 14A-D) occurs in two specific areas of the transect located in the central part of the basin (section CL; Fig. 4) and in the distalmost area of the foreland basin (INT section) (supplementary data). In these localities, the nodular breccia occurs atop the stratigraphic interval bearing calcite and quartz pseudomorphs or in an equivalent stratigraphic position. The basal contact of this breccia can be gradual or a sharp irregular surface cutting into the underlying strata. The pseudomorphs after gypsum of the strata underlying the nodular breccia may have geopetal infills containing well-preserved calcitized root fragments (Fig. 14E and F).

Facies I consists of clast- to matrix-supported nodular breccias composed of very poorly sorted calcareous intraclasts with gradual to sutured contacts within a grey to light ochre matrix (Fig. 14A). Pressure–solution features, such as sutured intraclast contacts and stylolites (also affecting the matrix), confer the nodular appearance to the breccias (Fig. 14A and B). Intraclasts comprise recrystallized radiolaria-bearing calci-mudstones, which commonly show scattered calcite pseudomorphs after gypsum (facies A and C; Fig. 14A and B). Breccia matrix is composed of micrite–microspar with chalcedony replacements (Fig. 14C), framboidal pyrite aggregates, and scattered small (20–25 µm) dolomite crystals at specific locations (Fig. 14D), the latter being particularly abundant near the undulated seams and stylolitic surfaces. Furthermore, well-preserved calcitized root fragments occur as a common feature in the matrix of nodular breccias (Fig. 14C).

Cathodoluminescence studies evidence the pervasive recrystallization of both the calcareous intraclasts and the matrix of the breccia. Microsparite from both the intraclasts and the matrix varies from non-luminescent to irregularly blotchy luminescent. Dolomite crystals in the breccia matrix show a characteristic pink luminescence, whereas root fragments show a bright yellow luminescence. In addition, the strata underlying the nodular breccias show increasing luminescence of the microsparite matrix towards the contact with the nodular breccias. The calcite pseudomorphs after gypsum in the layers underlying the nodular breccias show geopetal infills, in cases exhibiting root fragments and drusy equant-blocky calcite cements beginning with a thick non-luminescent overgrowth followed by orange luminescent overgrowths. The final pore filling stage shows a dull red luminescence (Fig. 14E, F).

Interpretation

Facies I and the underlying deposits show several features that suggest that the nodular breccia formed due to subaerial exposure of the underlying evaporite deposits. The geopetal infills of the gypsum moulds containing root fragments recognized in the underlying deposits indicate that the calci-mudstones with evaporitic gypsum crystals underlying the breccias were dissolved by meteoric waters and potentially colonized by plants. The nodular appearance of the breccia and intraclasts with diffuse to sharp edges resembles orthic and disorthic nodules described in calcretes studied by Wright (1982) (and references therein). The intense recrystallization of both the breccia matrix and the nodules is consistent with pedogenic processes. The meteoric features depicted a subaerial emergence of the evaporite deposits due to a major sea-level drop. Overall, the lack of large karstic dissolution features and the immature character of the observed pedogenic structures suggest that arid/semiarid climatic conditions prevailed during the time of exposure (cf. Esteban and Klappa, 1983).

5. DISCUSSION

5.1. Areal distribution of the mid-Carboniferous gypsum deposits in the North of Iberia

This study reveals an extensive distribution of mid-Carboniferous gypsum deposits along the studied exposures of the Variscan foreland basin, which significantly broadens the areal distribution depicted by González Lastra (1978) and Sánchez de la Torre and González Lastra (1978). Although the presence of calcite and quartz pseudomorphs after gypsum was never reported in time-equivalent strata in the Pyrenees, this study demostrates their presence in all the investigated outcrops (Aragón Subordán Valley, Canfranc and Aspe-Brousset Valley).

If only the current geographical distribution of studied exposures with reported calcite pseudomorphs after gypsum is considered, the estimated area with gypsum deposition would be of at least 61,000 km^2 taking into account the current axial length and width of the Variscan foreland fold and thrust belt where the pseudomorphs after gypsum are reported in this study (ca. 770 km in length – present-day distance from the southern outcrops of the CZ to the easternmost exposures in the Pyrenees – and ca. 70 km in width). However, the area where gypsum deposition took place increases significantly if the Variscan foreland thrust and fold belt is restored to its original size prior to thrusting and the oroclinal bending that led to the development of the Ibero-Armorican Arc. In the CZ, the tectonic shortening caused by the Variscan thrusting reached up to 70% (Alonso, 1987; Álvarez-Marrón and Pérez-Estaún, 1988; Bulnes and Marcos, 2001; Alonso et al., 2009), which implies that the original width of the preserved areas of the foreland basin in the CZ might have reached 250–300 km. If this width is considered along the 770 km-long axial strike of the foreland fold and thrust belt, a minimum areal extent under evaporite sedimentation of 231,000 km^2 is estimated. This areal estimate, which most likely represents a small fraction of the original area of the basin affected by hypersaline conditions, is comparable to the extension of saline giant deposits reported throughout the geological record (Warren, 2010, 2016). For comparison, Ferry Lake Anhydrite extends ca. 200,000 km^2 (Loucks and Longman, 1982; Warren, 2016) and the famous Permian Zechstein saline giant covered more than 600,000 km^2 (Geluk, 2000; Warren, 2016). The volume of gypsum and other evaporites accumulated in these saline giants is, however, considerably larger than in the case described in the present study. Nevertheless, it cannot be ruled out that the carbonate breccias (Facies H) occurring at the top of the stratigraphic interval containing pseudomorphs after gypsum could represent the relic of a vanished, larger evaporite accumulation, as it has been proposed in the literature for other breccias related with evaporite deposits (e.g., Nagy et al., 2005; Sorento, 2020).

5.2. A novel interpretation for gypsum deposits in the Variscan marine foreland basin

5.2.1. Relevant facts

Previous studies have interpreted the described deposits bearing calcite and quartz pseudomorphs after gypsum in the CZ as sabkha evaporites accumulated in shallow, restricted lagoon environments (González Lastra, 1978; Sánchez de la Torre and González Lastra, 1978; Eichmüller, 1985, 1986) based on the knowledge on carbonate and evaporite systems during the 1970s and 1980s. The new dataset presented in this study provides information on the spatial distribution and facies composition of the deposits bearing calcite and quartz pseudomorphs after gypsum in the Variscan foreland basin, allowing the revision of previous interpretations and the proposal of a new sedimentary scenario that may provide a plausible interpretation. To this end, the following facts are of paramount relevance:

a) Available biostratigraphic information on both conodonts and foraminifera suggests that the stratal package with calcite pseudomorphs after gypsum crystals has an early Baskhirian age. More specifically, it most probably would correlate with the Voznesenkian in the Donets Basin, Bogdanovkian in the South Urals, and Krasnopolyanian strata in the Moscow Basin. This interpretation is supported by the fact that these strata lie above the FAD of the conodonts *Declinognathodus inaequalis* and *Idiognathoides corrugatus*, first appearing in the Chokierian stage (Voznesenkian) (Barrick et al., 2021), and are, in turn, overlain by strata containing foraminifera compatible with a Syuranian (Voznesenkian/Bogdanovkian)–Krasnopolyanian age, in the case of the CQ section, and indicative of the Krasnopolyanian substage (upper Syuranian), in the case of the HV section. According to these data, the studied mid-Carboniferous strata with calcite and quartz pseudomorphs after gypsum in northern Spain are coeval with sabkha gypsum and anhydrite accumulations described in inter- to supratidal successions of the broad epeiric Sahara platform/shelf developed of northern Gondwana, which were connected to the distalmost realms of the Variscan basin: Tindouf (Middle and Upper Member of Ouarkziz Fm, Morocco; Mamet et al., 1966; Conrad, 1972a, b; Lys, 1988; Cózar et al., 2013, 2014a) and Reggan (Hassi Taïbine Gypsum Fm, Algeria; Conrad, 1984; Legrand-Blain 1985; Lys, 1988; Wendt et al., 2009; Legrand-Blain et al., 2010; Cózar et al., 2016), of late Serpukhovian–early Bashkirian age inferred primarily on the basis of reported foraminifera assemblages (Lys, 1988; Somerville et al., 2013, Cózar et al., 2014b) (Fig. 15).

b) The deposits bearing calcite and quartz pseudomorphs after gypsum in the Variscan foreland basin represent a minimum fraction of the potential size that the mid-Carboniferous evaporitic basin might have had in the likely event that the evaporitic strata of the epeiric Sahara platform/shelf represent the inter- to supratidal areasof the evaporitic system.

c) The stratigraphic thickness and facies composition of the deposits bearing calcite and quartz pseudomorphs after gypsum are extremely uniform across this huge domain of the Variscan foreland basin (Figs. 1B, 3 and 4), with predominance of intrasediment gypsum (mostly facies C and D; Fig. 8) and absence of selenite precipitates.

d) Sedimentologic data suggesting shallow subtidal to intertidal settings are absent across the investigated area. Instead, the microfacies underlying and hosting the studied pseudomorphs after intrasediment gypsums (see description and interpretation of facies A, C, D and E) suggest that evaporite precipitation took place in marine low-energy subtidal offshoreenvironments located below the local wave base. Furthermore, the evaporite-bearing deposits are interbedded and interfinger with turbidite deposits in the vicinity of the foredeep of the Variscan foreland basin. The exception would be the local subaerial exposure postdating the studied stratigraphic interval containing the calcite and quartz pseudomorphs after gypsum. The presence of this subaerial exposure horizon suggests that, at least locally, the deposition of the pseudomorph-bearing deposits took place in environments whose depth did not exceed the maximum amplitude of sea-level fall during mid-Carboniferous time, which could have reached up to 140 m (Rygel et al., 2008). The studied deposits are therefore interpreted as having formed in sublittoral below wave base to bathyal environments.

e) Although bioclasts are very scarce, radiolaria biomoulds are common along the studied succession, suggesting that environmental conditions were not too saline for pelagic biota at least in the upper portion of the water column..

5.2.2. Brine characteristics

The predominance of intrasediment gypsum growth in offshore environments requires the presence of hypersaline brines (more specifically, penesaline brines *sensu* Ortí, 2010a and Warren, 2016) in the interstitial pores at, or slightly underneath, the sediment–water interface (Handford, 1991; Warren, 2016). By comparison with studies in saltworks (Ortí et al., 1984; Bąbel, 2004; Ortí, 2010b, 2011), it can be interpreted that intrasediment gypsum (Facies C and D; Fig. 8) precipitated at salinities in seafloor around 140-150‰. Furthermore, higher brine concentrations (salinities around 150-230‰; cf. Ortí et al., 1984; Bąbel, 2004; Ortí, 2010b, 2011) could lead to the occasional precipitation of gypsum cumulates, which could settle down and accumulate on the bottom (Facies E; Fig. 10), as well as bottom-grown gypsum (Facies E and F; Figs. 10A, 11E, F). The upward increase in evaporite abundance and gradual reduction of gypsum crystal size , together with the increased abundance of gypsum cumulates and bottom-grown precipitates that occur in the studied stratigraphic interval, suggests an overall gradual increase in salinity during the evaporitic event. This salinity increase was probably accompanied by a relative sea-level fall that eventually produced the ephemeral emersion of the shallower areas of the Variscan foreland basin in the CZ (sections CL, INT; Figs. 3, 4 and supplementary data) that produced nodular breccias (facies I).

Despite their scarcity, the presence of planktonic organisms such as radiolaria in the carbonate matrix of facies C, D, E and F requires the vertical stratification of the water column, at least temporally, with near normal marine salinity above the pycnocline. Furthermore, intrasediment and bottom-grown gypsum precipitation and preservation of cumulate deposits, which is hampered in anoxic brines, point to relatively oxic conditions below the pycnocline.

5.2.3. Global context

The data presented in this study suggest that hypersaline conditions and evaporite deposition occurred nearly synchronously over large areas of the broad epeiric shelf of Gondwana and of the distal realms of the linked foreland basin facing the growing Ouachita–Alleghanian–Variscan Orogen. Inferred palaeolatitudes ranged from ca. 20º–24ºS for the coastal areas of the Saharan epeiric platform (Tindouf and Reggan successions in Morocco and Algeria) to ca. 9º–14º S for the coeval basinal areas in northern Spain and southern France (Scotese, 2001; Golonka, 2002; Scotese et al., 2014; Cao et al., 2017), lying within the high-density latitudinal belt of evaporites (with 50% confidence) for mid-Carboniferous times inferred by Cao et al. (2019). As a consequence of the closure of the connection of the Panthalassa and Palaeo-Tethys oceans, which some authors interpret to have occurred during the Serpukhovian–Bashkirian transition (see Blakey, 2008; Nance, et al. 2010; Davydov and Cózar, 2019), this area became a semi-enclosed basin. Furthermore, due to its palaeogeographical location in the westernmost embayment of the Palaeo-Tethys Ocean, it received the influx of saline subtropical warm waters pushed westward by trade winds, at a time when global mean sea-water salinities reached values around 45‰ as estimated by Hay et al. (2006) (Fig. 16B). In this context, the gradual narrowing of the associated foreland basin coupled with the globally recorded mid-Carboniferous long-term lowstand (Ross and Ross, 1987; Haq and Schutter, 2008; Rygel et al., 2008; Eros et al., 2012; Fig. 16A), probably increased basin restriction favouring gypsum precipitation in sublittoral below wave base to bathyal environments.

5.2.4. Basin model, proposed mechanisms for brine development

A sedimentary model providing a potential explanation for the widespread intrasediment gypsum precipitation documented in this study requires that the western part of the epeiric shelf of northern Gondwana and the Variscan foreland basin acted as a semi-closed basin system during the mid-Carboniferous lowstand (Fig. 17A). This scenario of a restricted connection with the Palaeo-Tethys Ocean and temporary or intermittent negative hydrological balance would have favoured hypersaline conditions and the development of supersaturated brines alternating with phases of lower salinity. In such a context, hydrological changes linked to variations in water input and evaporation rates would have caused significant changes in salinity and water stratification (see Bąbel, 2004).

Hypersaline water masses most likely developed in the shallow coastal regions of the margin of the foreland basin and/or across the vast epeiric Sahara Platform, where time-equivalent gypsum evaporite deposits accumulated (e.g. Tindouf and Reggan successions in Morocco and Algeria) (Fig. 17B). These deposits would potentially represent the shallow-water counterparts of the evaporite deposits described in this study. The shallow, dense hypersaline brines could have flown to deeper areas of the foreland basin, carrying the solutes needed to precipitate intrasediment evaporites. This mechanism could explain intrasediment gypsum precipitation over very broad areas of the marine basin, while surficial seawater could have shown near-normal marine salinities allowing planktonic biota, such as radiolaria, to thrive. Moreover, reaching salinities elevated enough for intrasediment gypsum precipitation (around 140-150‰) over such broad areas of the basin was probably favoured by the global high average salinities estimated for this time period (ca. 45‰) (see Hay et al., 2006; Valdes et al., 2021; Fig. 16B), as well as the major decoupling of water masses over Carboniferous epeiric platforms from the open ocean (see for example Montañez and Poulsen, 2018), particularly during mid-Carboniferous times (Brand et al., 2009).

A gradual decrease in water inflow: evaporation rate, probably linked to a relative sea-level fall (Fig. 17C), would eventually have produced the increase in salinity up to 150-230‰, necessary to precipitate, not only intrasediment gypsum (facies C and D), but also gypsum cumulates and bottom-growths (facies E and F2), which are more abundant in the upper part of the studied succession. The interbedding of gypsum laminae (either formed by cumulates, bottom-growths or intrasediment precipitates) with laminae composed of calci-mudstones to wackestones with scarce radiolaria in the upper part of the evaporitic interval studied suggests that, even during periods of higher salinities, the water column was separated into a surface water mass with lower salinity that enabled the presence of radiolaria and a deep-water mass with higher salinity (up to 150-230‰). Under such conditions, gypsum cumulates could precipitate either at the pycnocline or within the supersaturated brine and millimetre-thick bottom-grown gypsum crusts could form at the sea floor. Although complete mixing of the water column has been claimed for bottom growth of evaporites by some authors (see Warren, 2016), other authors have reported or modelled examples of bottom grown evaporites forming below the pycnocline in stratified water columns (Bąbel, 2004; Lugli et al., 2010; Sirota et al., 2016, 2017). The interpretation that the water column was stratified and gypsum (either bottom-grown, cumulates or intrasediment crystals) precipitated from the deep supersaturated brine seems more plausible than complete mixing of the water column during short-lived and recurrent episodes to explain the sedimentary features observed in the studied succession. The latter interpretation would require not only a very severe basin restriction but also longer time periods. However, it cannot be ruled out that during the final stages of the studied evaporitic event, and as a result of enhanced basin restriction during the mid-Carboniferous sea-level fall, the vertical mixing of the water column may have occurred. However, the widespread brecciation of the youngest strata of the studied evaporitic interval (leading to the development of facies H) prevents from obtaining additional information on the final stages of the evaporitic event.

The reduced amount of intrasediment evaporites in he sections near the foredeep of the basin (e.g., R section; Fig. 3 and 4) could be explained by a greater input of fresh water transported by gravity flows from the active Variscan Orogen. This would be consistent with the climatic zones modelled by Scotese et al. (2014), which define a tropical wet belt to the north of this marine basin. In addition, Reznik et al. (2009) observed that gypsum precipitation is adversely affected by clay minerals, which are not as good crystallization seeds as aragonite/calcite. Thus, a higher clay content in the deposits of the deeper parts of the foreland basin, transported from the orogen, could have inhibited/limited the formation of intrasediment gypsum. These gravity flows, including turbidity currents, probably reworked and transported gypsum crystals from shallower areas of the basin and led to the deposition of detrital gypsum-bearing beds (facies G).

Eventually, the mid-Carboniferous sea-level fall produced a short-lived and limited emersion of the shallower areas of the Variscan foreland basin in the CZ at the end of the evaporitic episode, leading to the erosion and subaerial weathering of gypsum bearing strata (facies I). This emersion could potentially be correlated with continental deposits (Série de la Betana in Tindouf Basin; Lys, 1988) and karstic surfaces (Béchar Basin; Lemosquet and Pareyn, 1975, 1983; Lys, 1988; Rygel et al., 2008) described in the Sahara Platform.

Wackestones, calci-mudstones, marlstone and detrital carbonates with diverse marine biota (Facies B) and coeval microbial boundstone bioconstructions (Fig. 2, 3B, 4; Eichmüller, 1985, 1986; Della Porta et al., 2003; Kenter et al., 2003; Bahamonde et al., 2007, 2015; Chesnel et al., 2016) were deposited atop of the evaporitic interval, suggesting that normal marine salinity conditions were restored in these areas of the basin during the subsequent sea-level rise.

5.2.5. Importance of the proposed scenario

The identification of gypsum precipitation in subtidal offshore (sublittoral below wave base to bathyal) sediments of the Variscan foreland basin, coeval with gypsum and anhydrite deposition in the epeiric shelf of Gondwana, suggests that a scenario of basin-wide evaporite precipitation could have developed during mid-Carboniferous times (early Bashkirian) in the marine areas between Gondwana and the Variscan Orogen. The development of such an extensive evaporitic area has not been reported so far, and sheds light on part of the evolution of the marine areas between Laurasia and Gondwana when the two continents collided. The proximity between the two approaching continents plus the mid-Carboniferous global sea-level lowstand may have restricted the surface connection of the foreland basin to the ocean. This, together with the fact that the basin was located at a palaeolatitude favourable to high evaporation rates (Cao et al., 2019), probably led to increase salinities and the development of a large saline basin, characterized by sabkha deposits in the peritidal areas of Gondwana shelf (Cózar et al., 2014a, 2014b, 2016) and by laminated calci-mudstone with intrasediment gypsum precipitates in subtidal offshore areas of the foreland basin of the CZ and the Pyrenees.

Although the origin of the laminated carbonates accumulated in offshore areas is still under investigation (see Merino-Tomé et al., 2021), the mechanism of gypsum precipitation has been determined in this study. One of the most interesting aspects of the pseudomorphs after gypsum crystals present within the subtidal offshore deposits of the CZ and the Pyrenees is that they correspond to originally intrasediment precipitates, because such precipitates are not common in deep marine sediments. Some of the few examples in the literature are syngenetic displacive gypsum crystals in Messinian deposits of the Mediterranean Basin (Fig. 3H in Lugli et al., 2015; Fig. 13A in Natalicchio et al., 2021), although in that case they co-occur with abundant cumulates, bottom-grown crystals, and reworked evaporites. The widespread presence of intrasediment gypsum in the Variscan foreland basin indicates that this type of evaporite growth is possible, and even dominant, in subtidal offshore environments and that it may have occurred in other ancient saline basins in the past. This study provides a model to explain gypsum precipitation in such distal areas, which involved brine descending from shallower areas (where intense evaporation took place) to subtidal offshore areas.

6. CONCLUSIONS

A remarkable mid-Carboniferous gypsum deposition event is recognised across broad areas of the Variscan foreland basin developed over Gondwana during the Pangea amalgamation, which is recorded as an up to 30 metre-thick stratigraphic package and may have reached an area of more than 231,000 km^2. Sedimentologic analyses provide evidence that intrasediment growth of gypsums occurred pervasively at, or slightly underneath, the sediment–water interface within carbonate muds accumulated in subtidal offshore environments (sublittoral below wave base to bathyal areas). Intrasediment gypsum abundance increases upwards, and coexists with gypsum cumulates and bottom-grown crystals in the upper part of the evaporitic interval. The gypsum evaporites recognized in the Variscan outcrops of northern Spain and southern France are coeval with gypsum deposits reported in the Saharan epeiric platform, which probably represented the shallow-water counterparts.

This early Bashkirian (Vozneseian) evaporitic interval recorded a major event of basin restriction in a marine foreland basin. In shallower coastal realms of the margin and/or across the vast epeiric Sahara Platform, restricted conditions and intense evaporation rates allowed the concentration of brines, which flowed to the deepest areas of the foreland basin. Intrasediment gypsum crystals began to grow within the calci-mudstone sediment as a result of deep brine supply. In the later stages of this event, sea-level fall favoured a gradual increase in salinity, which allowed the precipitation of bottom-grown gypsum and cumulates. This was followed by local subaerial exposures.

The evaporitic event took place during the mid-Carboniferous eustatic sea-level fall identified in different parts of the world, coeval with one of the highest salinity values for Phanerozoic seawaters. Although the mid-Carboniferous lowstand potentially enhanced basin restriction and most probably triggered gypsum precipitation in the Variscan foreland basin, the subsequent sea-level rise caused a return to normal marine conditions preventing the accumulation of larger volumes of evaporites in the basin.

DECLARATION OF COMPETING INTEREST

The authors declare that they have no known competing financial interests or personal relationships that could have appeared to influence the work reported in this paper.

ACKNOWLEDGEMENTS

This research has been supported by research projects CGL2013-46458-C2-1-R, CGL2013-44458-P and PGC2018-099698-B-I00 from the Spanish Government, SV-PA-13-ECOEMP-45, FC-GRUPIN-IDI/2018/000216 and AYUD/2021/51293 from the Principality of Asturias (FICYT), grants PAPI-19-PF-14 (University of Oviedo), PA-20-PF-BP19-139 (Principality of Asturias) and University of Oviedo – Santander Bank 2021-2022, and grant 160019 of the Swiss National Science Foundation. The work of E. Kulagina was carried out within the framework of the topic of the state task No. FMRS-2022-0010 (IG UFRC RAS). The authors are very grateful to F. Ortí for helpful discussion about the interpretation of the pseudomorphs after gypsum and the precipitation mechanisms. We would like to thank the two anonymous reviewers for their insightful comments, which improved the quality and clarity of the manuscript.

DATA AVAILABILITY

Supplementary figures can be found online at

REFERENCES

Aitken, J. D., 1967. Classification and Environmental Significance of Cryptalgal Limestones and Dolomites, with Illustrations from the Cambrian and Ordovician of Southwestern Alberta. SEPM Journal of Sedimentary

Research 37, 1163–1178. https://doi.org/10.1306/74D7185C-2B21-11D7-8648000102C1865D

Aigner, T., Bachmann, G.H., 1989. Dynamic stratigraphy of an evaporite-to-red bed sequence, Gipskeuper (Triassic), southwest German Basin. Sediment. Geol. 62, 5–25. https://doi.org/10.1016/0037-0738(89)90098-5

Aleksseev, A. S., Nikolaeva S.V., Goreva N.V., Donova, N.B., Kossovaya O.L., Kulagina, E.I., Kucheva, N.A., Kurilenko, A.V., Kutygin, R.V., Popeko, L. I. and Stepanova T. I. Russian regional Carboniferous stratigraphy. In: Lucas, S. G., Schneider, J. W., Wang, X. and Nikolaeva, S. (eds) The Carboniferous Timescale. Geological Society Special Publications 512 (1), 49–117. https://doi.org/10.1144/SP512-2021-134

Alimi, F., Gadri, A., 2004. Kinetics and morphology of formed gypsum. Desalination 166, 427–434. https://doi.org/10.1016/j.desal.2004.06.097

Alonso, J.L., 1987. Sequences of thrusts and displacement transfer in the superposed duplexes of the Esla Nappe Region (cantabrian zone, nw spain). J. Struct. Geol. 9, 969–983. https://doi.org/10.1016/0191-8141(87)90005-8

Alonso, J.L., Marcos, A., Suárez, A., 2009. Paleogeographic inversion resulting from large out of sequence breaching thrusts: The León Fault (Cantabrian zone, NW Iberia). A new picture of the external Variscan thrust belt in the Ibero-Armorican arc. Geol. Acta 7, 451–473. https://doi.org/10.1344/105.000001449

Alsharhan, A.S., Kendall, C.G.S.C., 2003. Holocene coastal carbonates and evaporites of the southern Arabian Gulf and their ancient analogues.

Earth-Science Rev. 61, 191–243. https://doi.org/10.1016/S0012-8252(02)00110-1

Álvarez-Marrón, J., Heredia, N., Pérez-Estaún, A., 1989. Mapa geológico de la Región del Ponga. Trab. Geol. 18, 127–135.

Álvarez-Marrón, J., Pérez-Estaún, A., 1988. Thin skinned tectonics in the Ponga region (Cantabrian Zone, NW Spain). Geol. Rundschau 77, 539–550. https://doi.org/10.1007/BF01832397

Aref, M. A., Taj, R. J., 2018. Recent evaporite deposition associated with microbial mats, Al-Kharrar supratidal–intertidal sabkha, Rabigh area, Red Sea coastal plain of Saudi Arabia. Facies 64, 28. https://doi.org/10.1007/s10347-018-0539-y

Bąbel, M., 1999. Facies and depositional environments of the Nida Gypsum deposits (Middle Miocene, Carpathian Foredeep, southern Poland). Geological Quaterly 43, 405–428.

Bąbel, M., 2004. Models for evaporite, selenite and gypsum microbialite deposition in ancient saline basins. Acta Geol. Pol. 54, 219–249.

Bahamonde, J.R., Merino-Tomé, Ó., Heredia, N., 2007. A Pennsylvanian microbial boundstone-dominated carbonate shelf in a distal foreland margin (Picos de Europa Province, NW Spain). Sediment. Geol. 198, 167–193. https://doi.org/10.1016/j.sedgeo.2006.12.004

Bahamonde, J.R., Merino-Tomé, O., Della Porta, G., Villa, E., 2015. Pennsylvanian carbonate platforms adjacent to deltaic systems in an active marine foreland basin (Escalada Fm., Cantabrian Zone, NW Spain). Basin Research 27, 208–229.

Bahamonde, J.R., Della Porta, G., Merino-Tomé, O., 2017. Lateral variability of shallow-water facies and high-frequency cycles in foreland basin carbonate platforms (Pennsylvanian, NW Spain). Facies 63, 1–39.

Barrick, J.E., Alekseev, A.S., Blanco-Ferrera, S., Goreva, N. V., Hu, K., Lambert, L.L., Nemyrovska, T.I., Qi, Y., Ritter, S.M., Sanz-López, J., 2022. Carboniferous conodont biostratigraphy. In: Lucas, S. G., Schneider, J. W., Wang, X. and Nikolaeva, S. (Eds), The Carboniferous Timescale. Geol. Soc. London, Spec. Publ. 512, 695–768. https://doi.org/10.1144/SP512-2020-38

Ben Dor, Y., Neugebauer, I., Enzel, Y., Schwab, M.J., Tjallingii, R., Erel, Y., Brauer, A., 2019. Varves of the Dead Sea sedimentary record. Quat. Sci. Rev. 215, 173–184. https://doi.org/10.1016/j.quascirev.2019.04.011

Blakey, R.C., 2008. Gondwana paleogeography from assembly to breakup—A 500 m.y. odyssey, in: In: Fielding, C.R., Frank, T.D., and Isbell, J.L., (Eds.), Special Paper 441: Resolving the Late Paleozoic Ice Age in Time and Space. Geological Society of America, pp. 1–28. https://doi.org/10.1130/2008.2441(01)

Bontognali, T.R.R., Vasconcelos, C., Warthmann, R.J., Bernasconi, S.M., Dupraz, C., Strohmenger, C.J., Mckenzie, J.A., 2010. Dolomite formation within microbial mats in the coastal sabkha of Abu Dhabi (United Arab Emirates). Sedimentology 57, 824–844. https://doi.org/10.1111/j.1365-3091.2009.01121.x

Brazhnikova, N.E., Vakarchuk, G.I., Vdovenko, M. V., Vinnichenko, L.V., Karpova, M.A., Kolomiets, Ya.I., Potievskaya, P.D., Rostovtseva, Shevchenko, G.D., 1967. Microfaunal marker reference horizons of

Carboniferous and Permian deposits from the Dnieper-Donets basin. “Naukova Dumka” Publ., Kiev, 224. (in Russian with English summary)

Brazhnikova, N.E., Potievska, P.D. 1948 Results of foraminiferal studies on borehole materials from the western edge of the Donbass, in Collection of Works in Paleontology and Stratigraphy: Akademiya Nauk Ukrains’koi RSR, Institut Geologichnikh Nauk, 1(2), 76-101. (in Ukrainian)

Brazhnikova, N.E., Jartzeva, M. V., 1956. On the question about the evolution of the genus Monotaxis. Voprosy Mikropaleontologii, 1: 62–68. (in Russian)

Bulnes, M., Marcos, A., 2001. Internal structure and kinematics of Variscan thrust sheets in the valley of the Trubia River (Cantabrian Zone, NW Spain): regional tectonic implications. Int. J. Earth Sci. 90, 287–303. https://doi.org/10.1007/s005310000138

Cao, W., Williams, S., Flament, N., Zahirovic, S., Scotese, C., Müller, D., 2019. Palaeolatitudinal distribution of lithologic indicators of climate in a palaeogeographic framework. Geol. Mag. 156, 331–354. https://doi.org/10.1017/S0016756818000110

Cao, W., Zahirovic, S., Flament, N., Williams, S., Golonka, J., Müller, R.D., 2017. Improving global paleogeography since the late Paleozoic using paleobiology. Biogeosciences 14, 5425–5439. https://doi.org/10.5194/bg-14-5425-2017

Chesnel, V., Merino-Tomé, Ó., Fernández, L.P., Villa, E., Samankassou, E., 2016. Isotopic fingerprints of Milankovitch cycles in Pennsylvanian carbonate platform-top deposits: the Valdorria record, Northern Spain. Terra Nov. 28, 364–373. https://doi.org/10.1111/ter.12229

Clifton, H.E., 1988. Sedimentologic Approaches to Paleobathymetry, with Applications to the Merced Formation of Central California. Palaios 3, 507–522.

Colmenero, J.R., Fernández, L.P., Moreno, C., Bahamonde, J.R., Barba, P., Heredia, N., González, F., 2002. Carboniferous, in: Gibbons, W., Moreno, M.T. (Eds.), The Geology of Spain. Geol. Soc. London, pp. 93–116. https://doi.org/10.1144/GOSPP.7

Conrad, J., 1972a. L’âge et les modalités de la régression carbonifère au bord nord du bassin de Tindouf (Sahara occidental). Comptes Rendus l’Académie des Sci. Paris 274, 1780–1783.

Conrad, J., 1972b. La régression namurienne sur le Nord de la plate-forme africaine. Comptes Rendus l’Académie des Sci. Paris 274, 2003–2006.

Conrad, J., 1984. Les séries carbonifères du Sahara central algérien: stratigraphie, sédimentologie, évolution structurale. Université d’Aix-Marseille.

Cózar, P., García-Frank, A., Somerville, I.D., Vachard, D., Rodríguez, S., Medina-Varea, P., Said, I., 2014a. Lithofacies and biostratigraphical correlation of marine Carboniferous rocks in the Tindouf Basin, NW Africa. Facies 60, 941–962. https://doi.org/10.1007/s10347-014-0409-1

Cózar, P., Medina-Varea, P., Somerville, I.D., Vachard, D., Rodríguez, S., Said, I., 2013. Foraminifers and conodonts from the late Viséan to early Bashkirian succession in the Saharan Tindouf Basin (southern Morocco): biostratigraphic refinements and implications for correlations in the western Palaeotethys. Geol. J. 49, 271–302. https://doi.org/10.1002/gj.2519

Cózar, P., Somerville, I.D., Blanco-Ferrera, S., Sanz-López, J., 2018. Palaeobiogeographic context in the development of shallow-water late Viséan-early Bashkirian benthic foraminifers and calcareous algae in the Cantabrian Mountains (Spain). Palaeogeogr. Palaeoclimatol. Palaeoecol. 511, 620–638. https://doi.org/10.1016/j.palaeo.2018.09.031

Cózar, P., Somerville, I.D., Vachard, D., Coronado, I., García-Frank, A., Medina-Varea, P., Said, I., Del Moral, B., Rodríguez, S., 2016. Upper Mississippian to lower Pennsylvanian biostratigraphic correlation of the Sahara Platform successions on the northern margin of Gondwana (Morocco, Algeria, Libya). Gondwana Res. 36, 459–472. https://doi.org/10.1016/j.gr.2015.07.019

Cózar, P., Vachard, D., Somerville, I.D., Medina-Varea, P., Rodríguez, S., Said, I., 2014b. The Tindouf Basin, a marine refuge during the Serpukhovian (Carboniferous) mass extinction in the northwestern Gondwana platform. Palaeogeogr. Palaeoclimatol. Palaeoecol. 394, 12–28. https://doi.org/10.1016/j.palaeo.2013.11.023

Davydov, V.I., Cózar, P., 2019. The formation of the Alleghenian Isthmus triggered the Bashkirian glaciation: Constraints from warm-water benthic foraminifera. Palaeogeogr. Palaeoclimatol. Palaeoecol. 531, 1–15. https://doi.org/10.1016/j.palaeo.2017.08.012

Della Porta, G., Kenter, J.A.M., Bahamonde, J.R., Immenhauser, A., Villa, E., 2003. Microbial boundstone dominated carbonate slope (Upper Carboniferous, N Spain): Microfacies, lithofacies distribution and stratal geometry. Facies 49, 175–207. https://doi.org/10.1007/s10347-003-0031-0

Demicco, R.V., Hardie, L.A., 1994. Sedimentary structures and early diagenetic features of shallow marine carbonate deposits. SEPM, Atlas Series. SEPM. https://doi.org/10.2110/sepmatl.01

Dietrich, B., 2005. Numerical Modeling as a Means to Enhance Genetic Sedimentary Basin Interpretation: A Case Study of the Southern Cantabrian Basin (NW Spain). Ph.D. thesis, Heildeberg University. DOI: 10.11588/heidok.00005729

Dott, R.H. Jr., Bourgeois, J., 1982. Hummocky stratification: significance of its variable bedding sequences. Geol. Soc. of America Bulletin 93, 663–680. https://doi.org/10.1130/0016-7606(1982)93<663:HSSOIV>2.0.CO;2

Dupraz, C., Visscher, P.T., Baumgartner, L. K., Reid, R. P., 2004. Microbe-mineral interactions: early carbonate precipitation in a hypersaline lake (Eleuthera Island, Bahamas). Sedimentology 51, 745–765. https://doi.org/10.1111/j.1365-3091.2004.00649.x

Eichmüller, K., 1985. Die Valdeteja Formation: Aufbau und Geschichte einer oberkarbonischen Karbonatplattform (Kantabrisches Gebirge, Nordspanien). Facies 13, 45–154. https://doi.org/10.1007/BF02536901

Eichmüller, K., 1986. Some Upper Carboniferous (Namurian; Westphalian). Lithostratigraphic Units in Northern Spain. Results and Implications of an Environmental Interpretation. Boletín Geológico y Min. 5, 590–607.

Eros, J.M., Montañez, I.P., Osleger, D.A., Davydov, V.I., Nemyrovska, T.I., Poletaev, V.I., Zhykalyak, M.V., 2012. Sequence stratigraphy and onlap history of the Donets Basin, Ukraine: Insight into Carboniferous icehouse dynamics. Palaeogeogr. Palaeoclimatol. Palaeoecol. 313–314, 1–25. https://doi.org/10.1016/j.palaeo.2011.08.019

Esteban, M., Klappa, C.F., 1983. Subaerial exposure environment, in: Scholle, P.A., Debout, D.G., Moore, C.H. (Eds.), Carbonate Depositional Environment, American Association of Petroleum Geologists, Memoir 33. American Association of Petroleum Geologists, pp. 2–95. https://doi.org/10.1306/M33429C1

Fernández, L.P., Bahamonde, J.R., Barba, P., Colmenero, J.R., Heredia, Nemesio, Rodríguez-Fernández, L.R., Salvador, C.I., Sánchez de Posada, L.C., Villa, E., Merino-Tomé, Ó., Motis, K., 2004. La sucesión sinorogénica de la Zona Cantábrica., in: Vera, J.A. (Ed.), Geología de España. SGE-IGME, Madrid, pp. 34–42.

Ferreira, T., Rasband, W., 2012. ImageJ User Guide. ImageJ/FIJI 1.46.

Flügel, E., 2004. Microfacies of Carbonate Rocks. Springer Berlin Heidelberg, Berlin, Heidelberg. https://doi.org/10.1007/978-3-662-08726-8

García-Sansegundo, J., Poblet, J., Alonso, J.L., Clariana, P., 2011. Hinterland-foreland zonation of the Variscan orogen in the Central Pyrenees: comparison with the northern part of the Iberian Variscan Massif. Geol. Soc. London, Spec. Publ. 349, 169–184. https://doi.org/10.1144/SP349.9

Geluk, M.C., 2000. Late Permian (Zechstein) carbonate-facies maps, the Netherlands. Netherlands J. Geosci. - Geol. en Mijnb. 79, 17–27. https://doi.org/10.1017/S0016774600021545

Gerdes, G., Krumbein, W.E., Noffke, N., 2000. Evaporite Microbial Sediments, in: Microbial Sediments. Springer Berlin Heidelberg, Berlin, Heidelberg, pp. 196–208. https://doi.org/10.1007/978-3-662-04036-2_22

Golonka, Jan, 2002. Plate-Tectonic maps of the Phanerozoic, in: Kiessling, W., Flugel, E., Golonka, J. (Eds.), Phanerozoic Reef Patterns. SEPM Society for Geology Special Publication 72. SEPM (Society for Sedimentary Geology), pp. 21–75. https://doi.org/10.2110/pec.02.72.0021

Golonka, J., Ross, M.I., Scotese, C.R., 1994. Phanerozoic paleogeographic and paleoclimatic modeling maps, in: Embry, A.F., Beauchamp, B., Glass, D.J. (Eds.), Pangea: Global Environments and Resources. Canadian Society of Petroleum Geologists, pp. 1–47.

González Lastra, J., 1978. Facies salinas en la caliza de montaña (Cordillera Cantábrica). Trab. Geol. 10, 249–265.

Grozdilova, L.P., Lebedeva, N.S., 1950. Some staffellid species from Middle Carboniferous deposits of the western slope of the Urals. Trudy Vsesoyuzhogo Neftyanogo Nauchno-Issledovatel'skogo Geologo-Razvedochnogo Instituta (VNIGRI), Mikrofauna SSSR Sbornik 3, Novaya Seriya 50, 5-45. (in Russian)

Handford, C.R., 1991. Marginal Marine Halite: Sabkhas and Salinas, in: Developments in Sedimentology. pp. 1–66. https://doi.org/10.1016/S0070-4571(08)70259-0

Haq, B.U., Schutter, S.R., 2008. A Chronology of Paleozoic Sea-Level Changes. Science 322(5898), 64–68. https://doi.org/10.1126/science.1161648

Hardie, L.A., Eugster, H.P., 1971. The depositional environment of marine evaporites: A case for shallow, clastic accumulation. Sedimentology 16, 187–220. https://doi.org/10.1111/j.1365-3091.1971.tb00228.x

Hay, W.W., Migdisov, A., Balukhovsky, A.N., Wold, C.N., Flögel, S., Söding, E., 2006. Evaporites and the salinity of the ocean during the Phanerozoic: Implications for climate, ocean circulation and life. Palaeogeogr. Palaeoclimatol. Palaeoecol. 240, 3–46. https://doi.org/10.1016/j.palaeo.2006.03.044

Heilbronner, R., Barrett, S., 2014. Image Analysis in Earth Sciences. Springer, Berlin, Heidelberg. https://doi.org/10.1007/978-3-642-10343-8

Hemleben, C., Reuther, C.-D., 1980. Allodapic limestones of the Barcaliente Formation (Namurian A) between Luna and Cea Rivers (Southern Cantabrian Mountains, Spain). Neues Jahrb. für Geol. und Paläontologie 159, 225–255.

Howchin, W., 1888. Additions to the Knowledge of the Carboniferous Foraminifera. Journal of the Royal Microscopical Society 8(4), 533–545. https://doi.org/10.1111/j.1365-2818.1888.tb01697.x

Hurst, A., Scott, A., Vigorito, M., 2011. Physical characteristics of sand injectites. Earth-Science Rev. 106, 215–246. https://doi.org/10.1016/j.earscirev.2011.02.004

Ivanova, R.M., 1988. Late Serpukhovian foraminifera of the eastern slope of the middle and southern Urals. In: I.M. Kolobova and L.I. Kozatsky (Eds.) Yezhegodnik vsesoyuznogo paleontologicheskogo obshchestva, V. 31. Leningrad, Nauka, Leningradskoye otdeleniye Pupl., 5-12. (in Russian)

Jordan, P., Nüesch, R., 1989. Deformation structures in the Muschelkalk anhydrites of the Schafisheim Well (Jura overthrust, northern Switzerland). Eclogae Geologicae Helveticae 82, 429–454.

Kendall, A.C., 1992. Evaporites, in: Walker, R.G., James, N.P. (Eds.), Facies Models: Response to Sea Level Change. Geological Association of Canada, pp. 375–409.

Kenter, J.A.M., Van Hoeflaken, F., Bahamonde, J.R., Bracco Gartner, G.L., Keim, L., Besems, R.E., 2003. Anatomy and lithofacies of an intact and seismic-scale Carboniferous carbonate platform (Asturias, NW Spain): Analogues of hydrocarbon reservoirs in the Pricaspian Basin (Kazakhstan), in: Zempolich, W.G., Cook, H.E. (Eds.), Paleozoic Carbonates of the Commonwealth of Independent States (CIS), SEPM Special Publication 77. SEPM (Society for Sedimentary Geology), pp. 181–203. https://doi.org/10.2110/pec.02.74.0181

Kirkland, D.W., Denison, R.E., Dean, W.E., 2000. Parent Brine of the Castile Evaporites (Upper Permian), Texas and New Mexico. J. Sediment. Res. 70, 749–761. https://doi.org/10.1306/2DC40935-0E47-11D7-8643000102C1865D

Kulagina E., Nikolaeva S., Pazukhin V., Kochetova, N.N., 2014. Biostratigraphy and lithostratigraphy of the Mid-Carboniferous boundary beds in the Muradymovo section (South Urals, Russia). Geological Magazine 151 (2), 269–298. https://doi.org/10.1017/S0016756813000599

Kulagina, E.I., Rumyantseva, Z.C., Pazukhin, V.N., Kochetova, N.N., 1992. Granitsa nizhnego–srednego karbona na Yuzhnom Urale i Srednem Tian-Shane [Lower–Middle Carboniferous Boundary in the South Urals and Middle Tien-Shan]. Moscow, Nauka Publ. 112 p. (in Russian)

Krestovnikov, V.N., Theodorovich, G.I., 1936. A new species of the genus Archaediscus from the Carboniferous of the Southern Urals. Byulleten' Moskovskogo Obshchedtva Ispytatelei propody, Otdelelenie Geologii, Moscow, 44, 86–90. (in Russian)

Legrand-Blain, M., 1985. North Africa — Brachiopods, in: Wagner, R.H., Winkler Prins, C.F., Granados, L.F. (Eds.), The Carboniferous of the World II: Australia, Indian Subcontinent, South Africa, South America and North Africa. Instituto Geológico y Minero de España/Empresa Nacional Adaro de Investigaciones Mineras S.A., Madrid, pp. 372–374.

Legrand-Blain, M., Aretz, M., Atif, K.F.T., 2010. Discussion of “Carboniferous stratigraphy and depositional environments in the Ahnet Mouydir area (Algerian Sahara)” by Wendt et al. (Facies 55(3):443–472, DOI 10.1007/s10347-008-0176-y). Facies 56, 471–476. https://doi.org/10.1007/s10347-010-0214-4

Lemosquet, Y., Pareyn, C., 1983. Middle Carboniferous transgression and its relation to Serpukhovian paleokarst in Béchar Basin, Algeria, in: 10th International Congress of Carboniferous Geology and Stratigraphy. Madrid, Spain, p. 184.

Lemosquet, Y., Pareyn, C., 1975. Karst et chenaux de ravinement dans le Carbonifèremarin du Bassin de Béchar, in: III Réunion Annual Des Sciences de La Terre, Montpellier. Montpellier, p. 230.

Leslie, A.B., Kendall, A.C., Harwood, G.M., Powers, D.W., 1996. Conflicting indicators of palaeodepth during deposition of the Upper Permian Castile Formation, Texas and New Mexico. Geol. Soc. London, Spec. Publ. 116, 79–92. https://doi.org/10.1144/GSL.SP.1996.116.01.09

Lotze, F., 1945. Zur Gliederung der Varisziden der Iberischen Meseta. Geotektonische Forschungen 6, 78–92.

Loucks, R.G., Longman, M.W., 1982. Lower Cretaceous Ferry Lake Anhydrite, Fairway Field, East Texas; product of shallow-subtidal deposition, in: Handford, C.R., Loucks, R.G., Davies, G.R. (Eds.), Depositional and Diagenetic Spectra of Evaporites; a Core Workshop. SEPM, Tulsa, OK, pp. 130–173.

Lugli, S., Manzi, V., Roveri, M., Schreiber, B.C., 2010. The Primary Lower Gypsum in the Mediterranean: A new facies interpretation for the first stage of the Messinian salinity crisis. Palaeogeogr. Palaeoclimatol. Palaeoecol. 297, 83–99. https://doi.org/10.1016/j.palaeo.2010.07.017

Lugli, S., Manzi, V., Roveri, M., Schreiber, B.C., 2015. The deep record of the Messinian salinity crisis: Evidence of a non-desiccated Mediterranean Sea. Palaeogeogr. Palaeoclimatol. Palaeoecol. 433, 201–218. https://doi.org/10.1016/j.palaeo.2015.05.017

Lys, M., 1988. Biostratigraphie du Carbonifère et du Permien en Mésogée (Espagne, Afrique du Nord, Régions égéennes, Proche-Orient): études micropaléontologiques (Foraminifères), paléobiogéographie. Bureau de Recherches Géologiques et Minières Paris, Documents du BRGM.

Magee, J.W., 1991. Late quaternary lacustrine, groundwater, aeolian and pedogenic gypsum in the Prungle Lakes, southeastern Australia. Palaeogeogr. Palaeoclimatol. Palaeoecol. 84, 3–42. https://doi.org/10.1016/0031-0182(91)90033-N

Malakhova, N.P., 1980. Assemblage of small foraminifera of the Middle Carboniferous of the southeastern Urals. USSR Academy of Sciences, Ural Scientific Center, A.N. Zavaritsky Institute of Geology and Geochemistry. Sverdlovsk, 53.

Mamet, B.L., Choubert, G., Hottinger, G., 1966. Notes sur le Carbonifère du Jebel Ouarkziz. Étude du passage du Viséen au Namurien d'après les foraminifères. Notes du Serv. Géologique du Maroc 27, 7–21.

Manzi, V., Gennari, R., Lugli, S., Persico, D., Roveri, M., Gavrieli, I. and Gvirtzman, Z. (2021) Synchronous onset of the Messinian salinity crisis and diachronous evaporite deposition: New evidences from the deep Eastern Mediterranean basin. Palaeogeogr. Palaeoclimatol. Palaeoecol. 584, 110685. https://doi.org/10.1016/j.palaeo.2021.110685

Martínez Catalán, J.R., Schulmann, K., Ghienne, J.-F., 2021. The Mid-Variscan Allochthon: Keys from correlation, partial retrodeformation and plate-tectonic reconstruction to unlock the geometry of a non-cylindrical belt. Earth-Science Rev. 220, 103700. https://doi.org/10.1016/j.earscirev.2021.103700

Merino-Tomé, Ó., Alonso, J.L., Bahamonde, J.R., Fernández, L.P., Marcos, A., Colmenero, J.R., Villa, E. and Suárez, A. (2019) Foreland Basin at the Cantabrian Zone: Evolution from the Distal Foreland Basin Successions to Wedge Top Deposition and the Tightening of the Ibero-Armorican Arc. In: Quesada, C. and Oliveira, J.T. (Eds.), The Geology of Iberia: A Geodynamic Approach, Volume 2: The Variscan Cycle, Regional Geology Reviews. Springer International Publishing, Cham, Switzerland, pp. 356–361. https://doi.org/10.1007/978-3-030-10519-8

Merino-Tomé, O., Gutiérrez-Alonso, G., Villa, E., Fernández-Suárez, J., Llaneza, J.M., Hofmann, M., 2017. LA-ICP-MS U-Pb dating of

Carboniferous ash layers in the Cantabrian Zone (N Spain): stratigraphic implications. J. Geol. Soc. London. 174, 836–849. https://doi.org/10.1144/jgs2016-119

Montañez, I.P., Osleger, D.J., Chen, J., Wortham, B.E., Stamm, R.G., Nemyrovska, T.I., Griffin, J.M., Poletaev, V.I., Wardlaw, B.R., 2018. Carboniferous climate teleconnections archived in coupled bioapatite δ18OPO4 and 87Sr/86Sr records from the epicontinental Donets Basin, Ukraine. Earth Planet. Sci. Lett. 492, 89–101. https://doi.org/10.1016/j.epsl.2018.03.051

Montañez, I.P., Poulsen, C.J., 2013. The Late Paleozoic Ice Age: An Evolving Paradigm. Annu. Rev. Earth Planet. Sci. 41, 629–656. https://doi.org/10.1146/annurev.earth.031208.100118

Monty, C.L.V., 1967. Distribution and structure of recent stromatolitic algal mats, Eastern Andros Island, Bahamas. Société Géologique de Belgique, Annales 90, 55–103.

Mulder, T., Alexander, J., 2001. The physical character of subaqueous sedimentary density flows and their deposits. Sedimentology 48, 269–299. https://doi.org/10.1046/j.1365-3091.2001.00360.x

Müller, W.H., Briegel, U., 1978. The rheological behaviour of polycrystalline anhydrite. Eclogae Geologicae Helveticae 71, 397–407.

Müller, W.H., Schmid, S.M., Briegel, U., 1981. Deformation experiments on anhydrite rocks of different grain sizes: rheology and microfabric. Tectonophysics 78, 527–543. https://doi.org/10.1016/0040-1951(81)90027-5

Nagy, Z.R., Somerville, I.D., Gregg, J.M., Becker, S.P., Shelton, K.L., 2005. Lower Carboniferous peritidal carbonates and associated evaporites adjacent to the Leinster Massif, southeast Irish Midlands. Geol. J. 40, 173–192. https://doi.org/10.1002/gj.999

Nance, R.D., Gutiérrez-Alonso, G., Keppie, J.D., Linnemann, U., Murphy, J.B., Quesada, C., Strachan, R.A., Woodcock, N.H., 2010. Evolution of the Rheic Ocean. Gondwana Res. 17, 194–222. https://doi.org/10.1016/j.gr.2009.08.001

Natalicchio, M., Pellegrino, L., Clari, P., Pastero, L., Dela Pierre, F., 2021. Gypsum lithofacies and stratigraphic architecture of a Messinian marginal basin (Piedmont Basin, NW Italy). Sediment. Geol. 425. https://doi.org/10.1016/j.sedgeo.2021.106009

Nemyrovska, T.I., Wagner, R.H., Winkler Prins, C.F., Montañez, I., 2011. Conodont faunas across the mid-carboniferous boundary from the barcaliente formation at la Lastra (Palentian Zone, Cantabrian Mountains, Northwest Spain); geological setting, sedimentological characters and faunal descriptions. Scr. Geol. 127–175.

Nikolaeva, S.V., Kulagina, E.I., Gorozhanina, E.N., Alekseev, A.S., Konovalova, V.A., 2017. Conodonts, ammonoids, foraminifers, and depositional setting of the Serpukhovian and Bashkirian stages in the Kugarchi Section in the South Urals, Russia. Stratigraphy, 14, 319–347.

Ortí, F., 2010a. Evaporitas: Introducción a la sedimentación evaporítica, in: Arche, A. (Ed.), Sedimentología. Del Proceso Físico a La Cuenca Sedimentaria. CSIC, pp. 675–769.

Ortí, F., 2010b. Evaporitas: Formaciones marinas y continentales. Algunos ejemplos, in: Arche, A. (Ed.), Sedimentología. Del Proceso Físico a La Cuenca Sedimentaria. CSIC, pp. 771–838.

Ortí, F., 2011. Selenite facies in marine evaporites: a review, in: Kendall, C.G.S.C., Alsharhan, A.S., Jarvis, I., Stevens, T. (Eds.), Quaternary Carbonate and Evaporite Sedimentary Facies and Their Ancient Analogues. A Tribute to Douglas James Shearman. Wiley, pp. 431–463. https://doi.org/10.1002/9781444392326.ch20

Ortí, F., Pueyo, J.J., Geisler-Cussey, D., Dulau, N., 1984. Evaporitic sedimentation in the coastal salinas of Santa Pola (Alicante, Spain). Rev. del Inst. Investig. Geol. la Diput. Barcelona (Universidad Barcelona) 38/39, 169–220.

Ortí, F., Rosell, L., Gibert, L., Moragas, M., Playà, E., Inglès, M., Rouchy, J.M., Calvo, J.P., Gimeno, D., 2014. Evaporite sedimentation in a tectonically active basin: The lacustrine Las Minas Gypsum unit (Late Tortonian, SE Spain). Sediment. Geol. 311, 17–42. https://doi.org/10.1016/j.sedgeo.2014.06.004

Paik, I.S., Huh, M., So, Y.H., Lee, J.E., Kim, H.J., 2007. Traces of evaporites in Upper Cretaceous lacustrine deposits of Korea: Origin and paleoenvironmental implications. J. Asian Earth Sci. 30, 93–107. https://doi.org/10.1016/j.jseaes.2006.07.013

Palache, C., Berman, H., Frondel, C., 1951. The system of Mineralogy. John Wiley and Sons.

Phillips, J., 1846. On the remains of microscopic animals in the rocks of Yorkshire. Proc. Geol. Polytech. Soc. West-Riding Yorksh. August 184, 274–302.

Postojalko, M.V., 1990. On the question of the boundary between the Lower and Middle Carboniferous in the Middle Urals. In: G.N. Papulov, and B.I. Chuvashov (Eds). Granitsy biostratigraficheskikh podrazdeleniy karbona Urala. Institut Geologii i Geokhimii Uralskogo Otdeleniya Akademii Nauk SSSR, Sverdlovsk, 71–92. (imprinted 1991) (in Russian)

Pratt, B.R., 2001. Calcification of cyanobacterial filaments: Girvanella and the origin of lower Paleozoic lime mud. Geology 29, 763–766. https://doi.org/10.1130/0091-7613(2001)029<0763:COCFGA>2.0.CO;2

Purser, B. H., Evans, G. 1973. Regional sedimentation along the Trucial coast, SE Persian Gulf, in: Purser, B.H. (Ed.), The Persian Gulf: Holocene carbonate sedimentation and diagenesis in a shallow epicontinental sea. Springer, pp. 211–231.

Quijada, I.E., Suarez-Gonzalez, P., Benito, M.I., Lugli, S., Mas, R., 2014. From carbonate–sulphate interbeds to carbonate breccias: The role of tectonic deformation and diagenetic processes (Cameros Basin, Lower Cretaceous, N Spain). Sediment. Geol. 312, 76–93. https://doi.org/10.1016/j.sedgeo.2014.07.006

Quijada, I.E., Suarez-Gonzalez, P., Benito, M.I., Mas, R., 2013. Depositional Depth of Laminated Carbonate Deposits: Insights From the Lower Cretaceous Valdeprado Formation (Cameros Basin, Northern Spain). J. Sediment. Res. 83, 241–257. https://doi.org/10.2110/jsr.2013.23

Rauser-Chernousova, D. M., 1937. Chapter 2: Upper Paleozoic foraminifers, in Rauser-Chernousova, D.M., and Fursenko, A.V., Guide to foraminifers from the oil-bearing regions of the USSR, Part 1: ONTI, NKTP, USSR, Glavnaya Redaktsiya Gorno-Toplivnoy Literatury, Leningrad-Moscow, 320 p. (in Russian).

Rauser-Chernousova, D.M., 1948a. Some new species of foraminifers from Lower Carboniferous deposits of the Moscow Basin. Akademiya Nauk SSSR, Trudy Instituta Geologicheskikh Nauk, Geologicheskaya Seriya (No. 19), vyp. 62, 227-238. (in Russian).

Rauser-Chernousova, D.M., 1948b. Materials on the foraminiferal fauna of the Carboniferous deposits of central Kazakhstan. Akademiya Nauk SSSR, Trudy Instituta Geologicheskikh Nauk, Geologicheskaya Seriya (No. 21), vyp. 66, 1-25. (in Russian).

Rauser-Chernousova, D.M., Gryzlova, N.D., Kireeva, G.D., Leontovich, G.E., Safonova, T.P., Chernova, E.I., 1951. Middle Carboniferous fusulinids of the Russian Platform and Adjacent Regions. Akademiya Nauk SSSR, Institut Geologicheskikh Nauk, Ministerstvo Neftyanoy Promyshlennosti SSSR. Moscow, Akademiya Nauk SSSR Publ., 380 p.

Reiss, A.G., Gavrieli, I., Rosenberg, Y.O., Reznik, I.J., Luttge, A., Emmanuel, S., Ganor, J., 2021. Gypsum precipitation under saline conditions: Thermodynamics, kinetics, morphology, and size distribution. Minerals 11, 141. https://doi.org/10.3390/min11020141

Reitlinger, E.A., 1949. Smaller foraminifers in the lower part of the Middle Carboniferous of the Middle Urals and Kama River region. Izvestiya

Akademii Nauk SSSR, Seriya Geologicheskaya, no. 6, p. 149-164 (in Russian).

Reitlinger, E.A., 1950. Foraminifers from Middle Carboniferous deposits in the central part of the Russian Platform (exclusive of the Family Fusulinidae): Akademiya Nauk SSSR, Trudy Instituta Geologicheskikh Nauk, Geologicheskaya Seriya (No. 47), Vyp. 126, 127 p. (in Russian).

Reitlinger, E.A. 1980, To the question of the boundary between the Bogdanovsky and Krasnopolyansky horizons (foraminifers of the Homoceras Zone). Voprosy Mikropaleontologii, vyp. 23, 23-38. (in Russian with English summary)

Reuther, C.-D., 1977. Das Namur im südlichen Kantabrischen Gebirge (Nordspanien). Klustenbewegungen und Faziesdifferenzierung im Übergang Geosynklinale- Orogen. Clausthaler Geol. Abhandlungen 28, 1–122.

Reznik, I.J., Gavrieli, I., Ganor, J., 2009. Kinetics of gypsum nucleation and crystal growth from Dead Sea brine. Geochim. Cosmochim. Acta 73, 6218–6230. https://doi.org/10.1016/j.gca.2009.07.018

Riding, R., 2000. Microbial carbonates: the geological record of calcified bacterial-algal mats and biofilms. Sedimentology 47, 179–214. https://doi.org/10.1046/j.1365-3091.2000.00003.x

Riding, R., 2008. Abiogenic, microbial and hybrid authigenic carbonate crusts: Components of Precambrian stromatolites. Geol. Croat. 61, 73–103. https://doi.org/10.4154/GC.2008.10

Ross, C.A., Ross, J.R.P., 1987. Late Paleozoic Sea Levels and Depositional Sequences. Cushman Found. Foraminifer. Res. Spec. Publ. 24, 137–149.

Rouchy, J.M., Monty, C., 2000. Gypsum Microbial Sediments: Neogene and Modern Examples, in: Microbial Sediments. Springer Berlin Heidelberg, Berlin, Heidelberg, pp. 209–216. https://doi.org/10.1007/978-3-662-04036-2_23

Rouchy, J.M., Pierre, C., Sommer, F., 1995. Deep-water resedimentation of anhydrite and gypsum deposits in the Middle Miocene (Belayim Formation) of the Red Sea, Egypt. Sedimentology 42, 267–282. https://doi.org/10.1111/j.1365-3091.1995.tb02102.x

Rouchy, J.M., Taberner, C., Peryt, T.M., 2001. Sedimentary and diagenetic transitions between carbonates and evaporites. Sediment. Geol. 140, 1–8. https://doi.org/10.1016/S0037-0738(00)00169-X

Rygel, M.C., Fielding, C.R., Frank, T.D., Birgenheier, L.P., 2008. The Magnitude of Late Paleozoic Glacioeustatic Fluctuations: A Synthesis. J. Sediment. Res. 78, 500–511. https://doi.org/10.2110/jsr.2008.058

Sánchez de la Torre, L., Águeda Villar, J.A., Colmenero Navarro, J.R., García-Ramos, J.C., González Lastra, J., 1983. Evolución sedimentaria y paleogeográfica del Carbonífero en la Cordillera Cantábrica, in: Martínez Díaz, C. (Ed.), Carbonífero y Pérmico de España. X Congreso Internacional de Estratigrafía y Geología Del Carbonífero. IGME, pp. 133–149.

Sánchez de la Torre, L., González Lastra, J., 1978. Esquema de la distribución de ambientes y facies sedimentarias en el Carbonífero Inferior de la Cordillera Cantábrica. Trab. Geol. 10, 401–406.

Sanz-López, J., 2019. Synorogenic Eastern Iberian Peninsula Basins Related to the Paleotethys Margin, in: Simancas, J.F., Quesada, C., Oliveira, J.T. (Eds.), The Geology of Iberia: A Geodynamic Approach. Volume 2: The Variscan Cycle, Regional Geology Reviews. Springer International Publishing, Cham, Switzerland, pp. 408–413. https://doi.org/10.1007/978-3-030-10519-8

Sanz-López, J., Blanco-Ferrera, S., 2012. Lower Bashkirian conodonts from the Iraty Formation in the Alduides-Quinto Real Massif (Pyrenees, Spain). Geobios 45, 397–411. https://doi.org/10.1016/j.geobios.2011.09.003

Sanz-López, J., Blanco-Ferrera, S., Sánchez de Posada, L.C., 2010. El límite Misisípico/Pensilvánico a partir del contenido en conodontos del estratotipo de la Formación Barcaliente (Zona Cantábrica), in: Libro de Resúmenes Del III Congreso Ibérico de Paleontología. Lisboa, pp. 289–292.

Sanz-López, J., Blanco-Ferrera, S., Sánchez de Posada, L.C., 2013. Conodont chronostratigraphical resolution and Declinognathodus evolution close to the Mid-Carboniferous Boundary in the Barcaliente Formation type section, NW Spain. Lethaia 46, 438–453. https://doi.org/10.1111/let.12021

Sanz-Montero, M.E., García, M.A., Rodríguez-Aranda, J.P., 2006. Facies dolomíticas de sistemas lacustres miocenos en las cuencas del Duero y de Madrid . Rasgos indicativos de su origen microbiano. Geo-Temas 9, 215–218.

Sanz-Montero, M.E., Rodríguez-Aranda, J.P., 2022. Seismites in Miocene gypsum microbialites: Multiproxy tools for paleoenvironmental reconstruction of saline lakes. Sediment. Geol. 439, 106219. https://doi.org/10.1016/j.sedgeo.2022.106219Schlager, W., Bolz, H., 1977. Clastic accumulation of sulphate evaporites in deep water. J. Sediment. Petrol. 47, 600–609. https://doi.org/10.1306/212F71F3-2B24-11D7-8648000102C1865D

Schmalz, R.F., 1969. Deep-Water Evaporite Deposition: A Genetic Model. Am. Assoc. Pet. Geol. Bull. 53, 798–823. https://doi.org/10.1306/5D25C7FD-16C1-11D7-8645000102C1865D

Scotese, C.R., 2001. Atlas of Earth History, Volume 1,. ed. PALEOMAP Project, Arlington, TX.

Scotese, C.R., Boucot, A.J., Chen, X., 2014. Atlas of Phanerozoic Climatic Zones (Mollweide Projection), Volumes 1-6, PALEOMAP Project PaleoAtlas for ArcGIS. PALEOMAP Project, Evanston, IL.

Sirota, I., Arnon, A., Lensky, N.G., 2016. Seasonal variations of halite saturation in the Dead Sea: Water Resources Research 52, 7151–7162. https://doi.org/10.1002/2016WR018974

Sirota, I., Enzel, Y., and Lensky, N.G., 2017, Temperature seasonality control on modern halite layers in the Dead Sea: In situ observations: Bulletin of the Geological Society of America 129, 1181–1194. https://doi.org/10.1130/B31661.1

Somerville, I.D., Cózar, P., Said, I., Vachard, D., Medina-Varea, P., Rodríguez, S., 2013. Palaeobiogeographical constraints on the distribution of foraminifers and rugose corals in the Carboniferous Tindouf Basin, South Morocco. J. Palaeogeogr. 2, 1–18. https://doi.org/10.3724/SP.J.1261.2013.00014

Son, C.S., Flemming, B.W., Chang, T.S., 2012. Sedimentary facies of shoreface-connected sand ridges off the East Frisian barrier-island coast, southern North Sea: climatic controls and preservation potential, in: Li, M.Z, Sherwood , C.R., Hill, P.R. (Eds), Sediments, Morphology and Sedimentary Processes on Continental Shelves: Advances in technologies, research and applications. Int. Assoc. Sedimentol. Spec. Publ. 44, pp. 143–158.

Sorento, T., Olaussen, S., Stemmerik, L., 2019. Controls on deposition of shallow marine carbonates and evaporites – lower Permian Gipshuken Formation, central Spitsbergen, Arctic Norway. Sedimentology 67, 207–238. https://doi.org/10.1111/sed.12640

Spadafora, A., Perri, E., Mckenzie, J.A., Vasconcelos, C., 2010. Microbial biomineralization processes forming modern Ca:Mg carbonate stromatolites. Sedimentology 57, 27–40. https://doi.org/10.1111/j.1365-3091.2009.01083.x

Suarez-Gonzalez, P., Arenas, C., Benito, M.I., Pomar, L., 2019a. Interplay between biotic and environmental conditions in pre-salt Messinian microbialites of the western Mediterranean (Upper Miocene, Mallorca, Spain). Palaeogeogr. Palaeoclimatol. Palaeoecol., 533, 109242. https://doi.org/10.1016/j.palaeo.2019.109242

Suarez-Gonzalez, P., Benito, M.I., Quijada, I.E., Mas, R., Campos-Soto, S., 2019b. ‘Trapping and binding’: A review of the factors controlling the development of fossil agglutinated microbialites and their distribution in space and time. Earth-Science Rev., 194, 182–215. https://doi.org/10.1016/j.palaeo.2019.109242

Tucker, M.E., 1990. Modern Carbonate Environments, in: Tucker, M.E., Wright, V.P. (Eds.), Carbonate Sedimentology. Blackwell Publishing Ltd., Oxford, UK, pp. 70–100. https://doi.org/10.1002/9781444314175.ch3

Tucker, M.E., 1991. Sequence stratigraphy of carbonate-evaporite basins: models and application to the Upper Permian (Zechstein) of northeast England and adjoining North Sea. J. Geol. Soc. London. 148, 1019–1036. https://doi.org/10.1144/gsjgs.148.6.1019

Tompson, M. L. (1944) Pennsylvanian Morrowan Rocks and Fusulinids of Kansas. Kansas Geological Survey, Bulletin. 52(7), 409-431.

Valdes, P.J., Scotese, C.R., Lunt, D.J., 2021. Deep ocean temperatures through time. Clim. Past 17, 1483–1506. https://doi.org/10.5194/cp-17-1483-2021

Villa, E., Sánchez de Posada, L.C., Fernández, L.P., Martínez-Chacón, M.L., Stavros, C., 2001. Foraminifera and biostratigraphy of the Valdeteja Formation stratotype (Carboniferous, Cantabrian Zone, NW Spain). Facies 45, 59–86. https://doi.org/10.1007/BF02668105

Warren, J.K., 2010. Evaporites through time: Tectonic, climatic and eustatic controls in marine and nonmarine deposits. Earth-Science Rev. 98, 217–268. https://doi.org/10.1016/j.earscirev.2009.11.004

Warren, J.K., 2016. Evaporites, A Geological Compedium. Springer International Publishing. https://doi.org/10.1007/978-3-319-13512-0

Wendt, J., Kaufmann, B., Belka, Z., Korn, D., 2009. Carboniferous stratigraphy and depositional environments in the Ahnet Mouydir area (Algerian Sahara). Facies 55, 443–472. https://doi.org/10.1007/s10347-008-0176-y

Winkler Prins, C.F., 1971. The road section East of Valdeteja with its continuation along the Arroyo de Barcaliente (Curueño Valley, Leon). Trab. Geol. 4, 677–686.

Wright, V.P. 1982. Calcrete palaeosols from the lower carboniferous Llanelly formation, South Wales. Sedimentology 33, 1–33. https://doi.org/10.1016/0037-0738(82)90025-2

Zeller, D. E. N. (1953) Endothyroid Foraminifera and ancestral fusulinids from the type Chesteran (Upper Mississippian). Journal of Paleontology. 27(2), 183–199.

FIGURE CAPTIONS

Figure 1. A) Palaeographic reconstruction of the southern intertropical area of Pangea during mid-Carboniferous times (≈323 My) showing the location of the studied deposits with pseudomorphs after gypsum of the Variscan foreland basin (N Spain and S France), and potentially time equivalent gypsum strata of N Gondwana. Redrawn from Golonka et al. (1994), Scotese (2001) and Golonka (2002). **B)** Sketch showing the configuration of the Variscan massifs of Iberia prior to the opening of the Bay of Biscay (modified after Martínez Catalán et al., 2021) with location of the 67 studied outcrops. The boundary between the internal

areas of the Variscan orogen and the foreland fold and thrust belt in the Pyrenees has been drawn according to García-Sansegundo et al. (2011).

Figure 2. Chronostratigraphic diagram for mid-Carboniferous strata of the CZ and Pyrenees (modified from Sanz-López and Blanco-Ferrera, 2012; Merino-Tomé et al., 2017, 2019; Cózar et al., 2018; Sanz-López, 2019).

Figure 3. A) Synthetic map of the CZ showing the areal distribution of the Barcaliente Formation and the localities in which calcite and quartz pseudomorphs after gypsum have been observed or reported in the literature. **B)** Stratigraphic cross section showing the Mississippian and Early Pennsylvanian succession of the southern branch of the CZ (see location in A, red line).

Figure 4. Correlation of the sedimentary facies of the upper part of the Barcaliente Fm and the overlying deposits along the cross section shown in figure 3B. A log of the estimated abundance of calcite and quartz pseudomorphs after gypsum is shown for the Porma Reservoir section (P).

Figure 5. Selected taxa of foraminifera recorded in samples from the CQ section (see Fig. 14). Scale bar is 0.2 mm for each image. **1)** *Semiendothyra* cf. *tumulifera* (Reitlinger, 1980), almost axial section, Spl. CE-440. **2)** *Planoendothyra* aff. *inusitata* (Reitlinger, 1950), axial section, Spl. CE-440. **3)** *Endothyra* ex gr. *bowmani* (Phillips, 1846), Spl. CE-450. **4)** *Ikensieformis postproikensis* (Brazhnikova, 1967), axial section, Spl. CE-406. **5)** *Eostaffella exilis* (Grozdilova and Lebedeva, 1950), axial section, Spl. CE-398. **6)** *Eostaffellina* ex gr. *paraprotvae* (Rauser-Chernousova, 1948), close to axial section, Spl. CE-434. **7)** *Ikensieformis* cf. *proikensis* (Rauser-Chernousova, 1948a), axial section, Spl. CE-440. **8)** *Eostafella acutiformis* Kireeva in Rauser-Chernousova et al., (1951),

almost axial section, Spl. CE-406. **9)** *Plectostaffella* sp., median section, Spl. CE-419B. **10)** *Ikensieformis* cf. *mirifica* (Brazhnikova in Brazhnikova et al., 1967), tangential section, Spl. CE-402. **11, 12)** *Eostafella statuta* Reitlinger, 1980, axial sections, both from Spl. CE-440. **13)** *Neoarchaediscus* sp., oblique section, Spl. CE-398. **14)** *Eostafella* sp., axial section, Spl. CF-7. **15)** *Monotaxinoides transitorius* (Brazhnikova and Jartzeva, 1956), axial section, CE-440. **16)** *Neoarchaediscus regularis* (Suleimanov, 1948), axial section, Spl. CF-7. **17)** *Rugosoarchaediscus karreriformis* (Reitlinger, 1950), axial section, CE-405. **18, 19)** *Asteroarchaediscus bashkiricus* (Krestovnikov and Theodorovich, 1936); 18 – median section, Spl. CE-398; 19 –section close to axial, Spl. CE-419B. **20)** *Howchinia sp.,* oblique section, Spl. CE-396.2. **21)** *Bradyina cribrostomata* (Rauzer-Chernousova and Reitlinger, 1937), median section, Spl. CE-419B. **22)** *Janischewskina* sp., tangential section, Spl. CE-402. **23)** *Howchinia bradyana* (Howchin, 1888 = *Howchinia gibba longa* Brazhnikova in Brazhnikova et al., 1967), axial section, Spl. CE-396.2.

Figure 6. Selected foraminifera of the HV Section. Scale bar = 0.2 mm. **1)** *Calcitornella* sp., Spl., HVB-92.2. **2)** *Eolasiodiscus donbassicus* (Reitlinger, 1956), axial section, Spl. HV1-18. **3)** *Monotaxinoides* cf. *priscus* (Braznikova and Jartseva, 1956), axial section, Spl. HV1-18. The test is silicified. **4)** *Hemidiscopsis muradymicus* (Kulagina in Kulagina et al., 1992), tangential section, Spl. HVB-93. **5)** *Eolasiodiscus* sp., axial section, Spl. HVB-92.2. **6, 7)** *Asteroarchaediscus bashkiricus* (Krestovnikov et Theodorovich, 1936), axial sections: both from Spl. HV1-18. **8)** *Asteroarchaediscus rugosus* (Reitlinger, 1949), axial section, Spl. HV1-18. **9)** *Monotaxinoides* cf. *transitorius* (Brazhnikova and Jartseva, 1956),

near-equatorial section, Spl. HVAL2-1. **10)** *Monotaxinoides gracilis* (Dain in Reitlinger, 1956), Spl. HVAL2-1. **11)** ?*Hemidiscopsis* sp., Spl. HVAL2-1, axial section. The test is partly silicified. **12, 13)** *Neoarchaediscus postrugosus* (Reitlinger, 1949), axial sections: 12 – Spl. HV1-18, 13 – HVB-93. **14)** *Neoarchaediscus borealis* (Reitlinger, 1949), axial section, Spl. HV1-18. **15)** *Monotaxinoides transitorius* (Brazhnikova and Yartseva, 1956) axial section, Spl. HVB-92.7B). The test is silicified. **16)** *Haplophragmina repens* (Malakhova, 1980), longitudinal section, Spl. HVAL2-1. **17)** *Eolasiodiscus* cf. *donbassicus* (Reitlinger, 1956), equatorial section, Spl. HV1-18. **18, 20)** *Biseriella glomerata* (Ivanova, 1988): 18 – section of the initial part of the shell passing through the proloculus, Spl. HV1-18, 20 – close to median section, Spl. HVAL2-0. **19)** *Biseriella* cf. *eogranulosa* (Reitlinger, 1949), section of the initial part of the shell, Spl. HV1-18. **21)** *Planoendothyra* aff. *irinae* (Reitlinger, 1950), axial section, HVAL2-1. **22)** *Endothyra* sp., close to axial section, Spl., HV1-18. **23)** *Endothyra phrissa* (Zeller, 1953), median section, HV1-18. **24)** *Planoendothyra* aff. *inusitata* (Reitlinger, 1950), axial section, Spl. HVAL2-1. **25)** *Eostaffellina paraprotvae* (Rauser-Chernousova, 1948), Spl. HV1-18. **26, 27)** *Eostaffella postmosquensis* (Kireeva in Rauser-Chernousova 1951), axial sections: both from Spl. HVB-93. **28)** *Eostaffella* cf. *parastruvei* (Rauser-Chernousova, 1948b), axial section, Spl. HVAL2-0. **29)** *Parastaffella* cf. *utkaensa* (Postojalko, 1990), tangential section, Spl. HVAL2-0. **30)** *Eostaffella* cf. *suranensis* (Reitlinger, 1980), tangential section, Spl. HVAL2-1. **31)** *Eostaffella* ex gr. *pseudostruvei* (Rauser-Chernousova and Belyaev *in* Rauser-Chernousova et al., 1936), oblique section, Spl. HVAL2-1. **32)** *Plectostaffella* cf. *varvariensis* (Brazhnikova and Potievska, 1948), oblique sections, HVB-93. **33)** Eostaffella cf. *pinguis* (Tompson, 1944), almost axial section, Spl. HVAL2-0.

Figure 7. Transmitted light photomicrographs of facies A and B. **A)** Burrowed calci-mudstone with disperse calcite biomoulds of radiolaria (r) (facies A). **B)** Pyritized radiolarian test preserving the internal structure (facies A). **C)** Dark-grey radiolarian wackestones (facies B) with abundant radiolarian biomoulds (r). **D)** Close-up view of radiolarian tests (r) preserving some of their spines in facies B.

Figure 8. A) Polished slab of facies C showing millimetre- to centimetre-sized lenticular calcite (Cal) and quartz (Q) pseudomorphs after gypsum (white arrows), locally forming centimetre-sized aggregates. **B and C)** Transmitted light microphotographs of facies C collected in the CZ (B) and Pyrenees (C). Pseudomorphs after gypsum show monoclinic prismatic and hexagonal sections (white arrows). **D)** Transmitted light photomicrograph of laminated calci-mudstones alternating with submillimetre-sized laminae of aggregates of calcite pseudomorphs after gypsum (facies D).

Figure 9. A) Histograms of crystal size distribution (CSD) of the calcite and quartz pseudomorphs obtained by area counting procedure in samples of facies C and D from Gamoniteiro (G), Viego (VI) and Porma Reservoir (P) sections (see Fig. 4A for location). **B)** Synthetic table showing calculated area equivalent diameter (D_E; range, mode and mean values) and mean Feret diameter (D_F, caliper or b axis) of the pseudomorphs calculated for samples of facies C and D of the aforementioned sections. **C)** Histogram showing pseudomorph abundance (% of area) and frequency (% of samples) in facies C and D (including samples from all the studied sections). Quantification was made by visual estimation and point and area counting procedures. Note that samples from facies C show generally

pseudomorph abundances ≤20%, whereas abundances from facies D overcome 20%.

Figure 10. A) Scanned thin section of facies E composed of laminae of calcite pseudomorphs after gypsum cumulates (1, 2, 3). Note the upward increase in the abundance of pseudomorphs within each pseudomorph-rich lamina. Pseudomorph lamina 1 shows a sharp upper contact and primary crystal terminations, which may have been formed by overgrowth of the cumulate crystals after their settling in the bottom. Py, pyrite replacements; st, stylolite; b, burrow. **B)** Photomicrograph showing cumulate cycles 2 and 3 from image A. The upper contact of the pseudomorph-rich lamina is stylolitized (st).

Figure 11. A) Outcrop image of subfacies F1 showing crinkly lamination. **B-D)** Transmitted light photomicrographs of subfacies F1. **B)** Dark micritic-microsparitic laminae with abundant radiolarian biomoulds and pores cemented by blocky calcite. **C)** Laminated microsparite with common radiolarian biomoulds (r) showing small, elongated pores parallel to lamination and cm-sized calcite pseudomorphs after lenticular gypsum. **D)** Detail of the microsparitic matrix of subfacies F1 that shows irregular porosities sub-parallel to lamination and contains radiolarian biomoulds (r). **E)** Scanned thin section of facies F2 showing calcite pseudormorphs of bottom-grown gypsum crystals (e), which show subhedral habits at the top of the laminae. Note the potential pseudomorphs after cumulates (c) near the top of the image. **F)** Detail of image E showing a calcite pseudomorph (e) after a bottom-grown gypsum crystal overlain by a dark micrite-microspar lamina with filamentous structures (f) resembling microbe moulds.

Figure 12. A) Centimetre-thick, medium to fine sand-grained arenite layer (facies G), interbedded with dark-grey calci-mudstones (facies A) and calci-mudstones

with scattered calcite pseudomorphs after intrasediment gypsum (facies C). **B)** Centimetre-thick arenite layer (facies G) with irregular erosive base and ripple cross-lamination. **C-E)** Transmitted-light photomicrographs of arenites with calcite pseudomorphs after detrital gypsum (facies G). **C)** Detail of the arenite shown in image A. Main components include sand-sized quartz grains (Q) and calcite pseudomorphs after detrital gypsum grains (e) showing abraded sub-euhedral monoclinic and lenticular habits. **D and E)** Arenites mainly composed of calcareous grains and calcite pseudomorphs after abraded grains with sub-euhedral and lenticular morphologies (white arrows), interpreted as being originally detrital gypsum grains.

Figure 13. A-C) Scanned thin sections of facies H consisting of breccia fragments composed of micritic limestone with calcite pseudomorphs after gypsum (e), embedded within a matrix composed of submillimetre-sized microsparite fragments. **D)** SEM image (backscattered electrons) showing a detail of the matrix shown in image C with common quartz replacements (Q). Quartz contains numerous rectangular solid inclusions of anhydrite (Anh) and corroded calcite (Cal). Mineralogy was confirmed by EDS analyses. **E)** Transmitted light photomicrograph of a quartz replacement (Q) affecting the breccia matrix composed by calcite (Cal). Quartz shows solid inclusions of anhydrite (Anh).

Figure 14. A and B) Scanned polished slab (image A) and thin section (image B) of facies I, a nodular breccia with centimetre-sized carbonate intraclasts with scattered calcite pseudomorphs after gypsum (e). Note sutured contacts of intraclasts, abundant stylolitic surfaces and common gradual contacts between the clasts and the matrix, which are characteristic features of orthic nodules. **C)** Photomicrograph of the breccia matrix showing a root fragment (rt). Cell walls of

the plant root tissues are replaced by micrite allowing the recognition of the xylem and the floem. Chalcedony (Chc) masses replace partially the matrix and the root structure. **D)** Photomicrograph of microsparitic matrix from a stained thin section exhibiting dolomite crystals (Dol) within the calcite matrix. **E and F)** Transmitted light (image E) and cathodoluminescence (image F) photomicrographs from a stratum underlying facies I, which is composed by mudstone with scattered calcite pseudomorphs after evaporites (facies C). Note that the lower part of the evaporite mould shows microsparite geopetal infill (g) with numerous root fragments (rt) and the upper part of the mould is filled by a banded drusy calcite cement (dr). The surrounding microsparitic matrix, which shows few radiolarian biomoulds (r), is blotchy and poorly luminescent, whereas the microspar of the geopetal infill shows brighter luminescence.

Figure 15. Biostratigraphic correlation of studied successions in the Cantabrian Mountains (QC and HV sections) and time equivalent successions from the Sahara Platform (Tindouf and Reggan sections) with representation of the FAD of key foraminifera markers (1–23), conodonts (24–27), brachiopods (28, 29), and corals (30). Conodont FADs of HV section based on Sanz-López et al. (2010, 2013) and *Pseudostaffella sp.* based on Villa et al. (2001). Stratigraphic columns and FADs of key foraminifera, conodonts, brachiopods and corals from Tindouf and Reggan modified from Lys (1988) and Cózar et al. (2013, 2016). New FAD of foraminifera from CQ and HV sections from this study. Substages/horizons of the upper Serpukhovian–lower Bashkirian and foraminifera and conodont biozones defined in the Southern Urals from Kulagina et al. (2014) and Nikolaeva et al. (2017); subdivisions of the East European Platform are after Alekseev et al. (2022).

Figure 16. A) Coastal onlap in the Donets Basin (Eros et al., 2012) and in the US Midcontinent (Ross and Ross, 1987), and amplitude of high-frequency sea-level glacio-eustasy from Middle Mississippian to Early Pennsylvanian times (Rygel et al., 2008). Redrawn from Montañez and Poulsen (2013). Gypsum deposits of Barcaliente Fm and equivalent stratigraphic units (orange arrow) are coeval with the major sea-level fall recorded in Donets Basin, US Midcontinent and other basins from around the world (orange area). **B)** Evolution of seawater salinities for the Phanerozoic Eon after Hay et al. (2006). Estimated mean seawater salinities for the mid-Carboniferous could have been as high as 45‰; the orange arrow indicates the inferred age of the studied evaporite interval.

Figure 17. Sedimentary scenario proposed for evaporite deposition in the Variscan foreland basin and Sahara epeiric platform. **A)** Palaeographic reconstruction of the southern intertropical area of Pangea during Late Serpukhovian – Early Bashkirian times (ca. 323 My) and a hypothetic cross section across the basin showing the relative location of the Variscan exposures of N Iberia (CZ and P) and the outcrops from the Saharan Platform (SP) where extensive evaporitic sedimentation occurred. **B)** Intense evaporation in shallow areas of the basin (e.g. the Saharan Platform) developed brines that flowed down into the lower part of the water column in subtidal offshore zones, leading to precipitation of mainly intrasediment evaporites. A pycnocline/halocline separating a normal-marine surficial water mass, which overlies the deep brine, allowed radiolaria to inhabit this epeiric sea. **C)** In advanced stages, a relative sea-level fall resulted in a more restricted basin and higher salinities, which led to precipitation of more abundant intrasediment gypsum, cumulates and bottom-grown crystals. **D)** Finally, sea-level drop led to local subaerial exposure. The

character of the water column during this final stage is not interpreted due to the lack of information.

Graphical abstract

HIGHLIGHTS

- Gypsum precipitation occurs in mid-Carboniferous offshore of a Variscan foreland basin
- These evaporites are broadly distributed marine deposits indicating a regional evaporitic event
- The proposed model provides new light into Carboniferous marine evaporite deposition

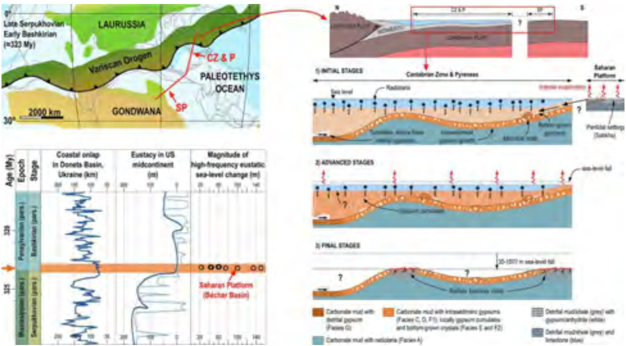

Graphics Abstract

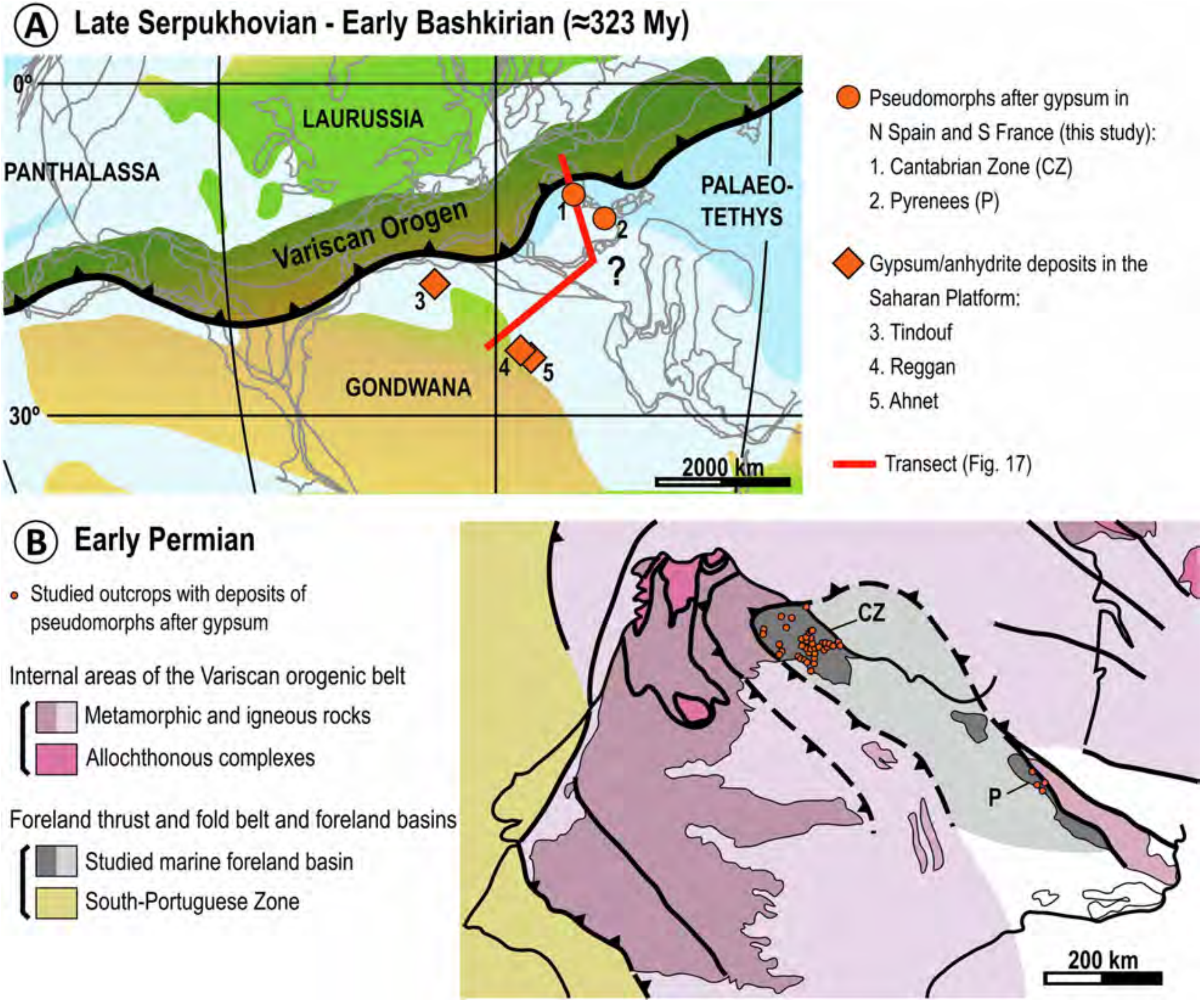
A
Late Serpukhovian - Early Bashkirian (≈323 My)
0°
30°
PANTHALASSA
LAURUSSIA
Variscan Orogen
PALAEO-TETHYS
GONDWANA
1
2
3
4
5
?
2000 km
Pseudomorphs after gypsum in N Spain and S France (this study):
1. Cantabrian Zone (CZ)
2. Pyrenees (P)
Gypsum/anhydrite deposits in the Saharan Platform:
3. Tindouf
4. Reggan
5. Ahnet
Transect (Fig. 17)
B
Early Permian
Studied outcrops with deposits of pseudomorphs after gypsum
Internal areas of the Variscan orogenic belt
Metamorphic and igneous rocks
Allochthonous complexes
Foreland thrust and fold belt and foreland basins
Studied marine foreland basin
South-Portuguese Zone
CZ
P
200 km

Figure 1

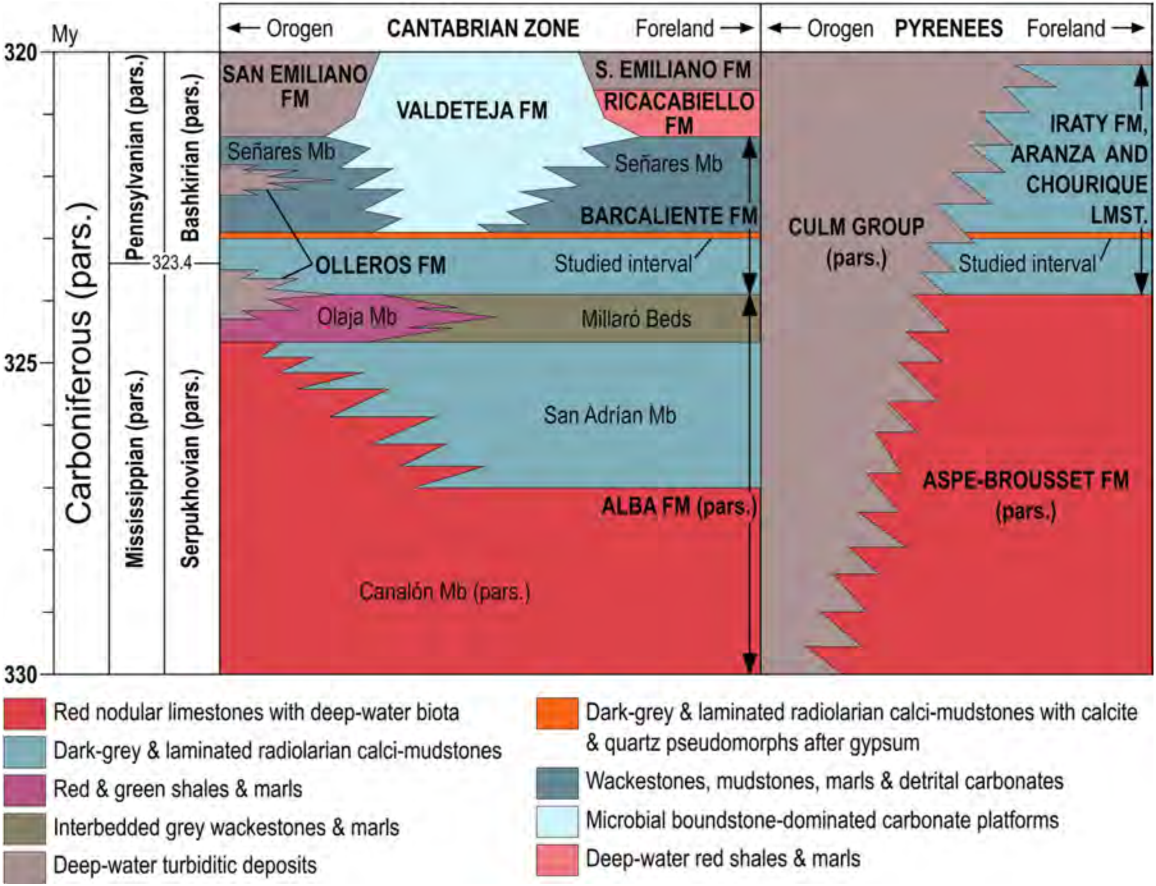
My
320
325
330
Carboniferous (pars.)
Pennsylvanian (pars.)
Missisippian (pars.)
Bashkirian (pars.)
Serpukhovian (pars.)
323.4
← Orogen
CANTABRIAN ZONE
Foreland →
← Orogen
PYRENEES
Foreland →
SAN EMILIANO FM
VALDETEJA FM
S. EMILIANO FM
RICACABIELLO FM
Señares Mb
Señares Mb
BARCALIENTE FM
OLLEROS FM
Studied interval
Olaja Mb
Millaró Beds
San Adrían Mb
ALBA FM (pars.)
Canalón Mb (pars.)
CULM GROUP (pars.)
IRATY FM, ARANZA AND CHOURIQUE LMST.
Studied interval
ASPE-BROUSSET FM (pars.)
Red nodular limestones with deep-water biota
Dark-grey & laminated radiolarian calci-mudstones
Red & green shales & marls
Interbedded grey wackestones & marls
Deep-water turbiditic deposits
Dark-grey & laminated radiolarian calci-mudstones with calcite & quartz pseudomorphs after gypsum
Wackestones, mudstones, marls & detrital carbonates
Microbial boundstone-dominated carbonate platforms
Deep-water red shales & marls

Figure 2

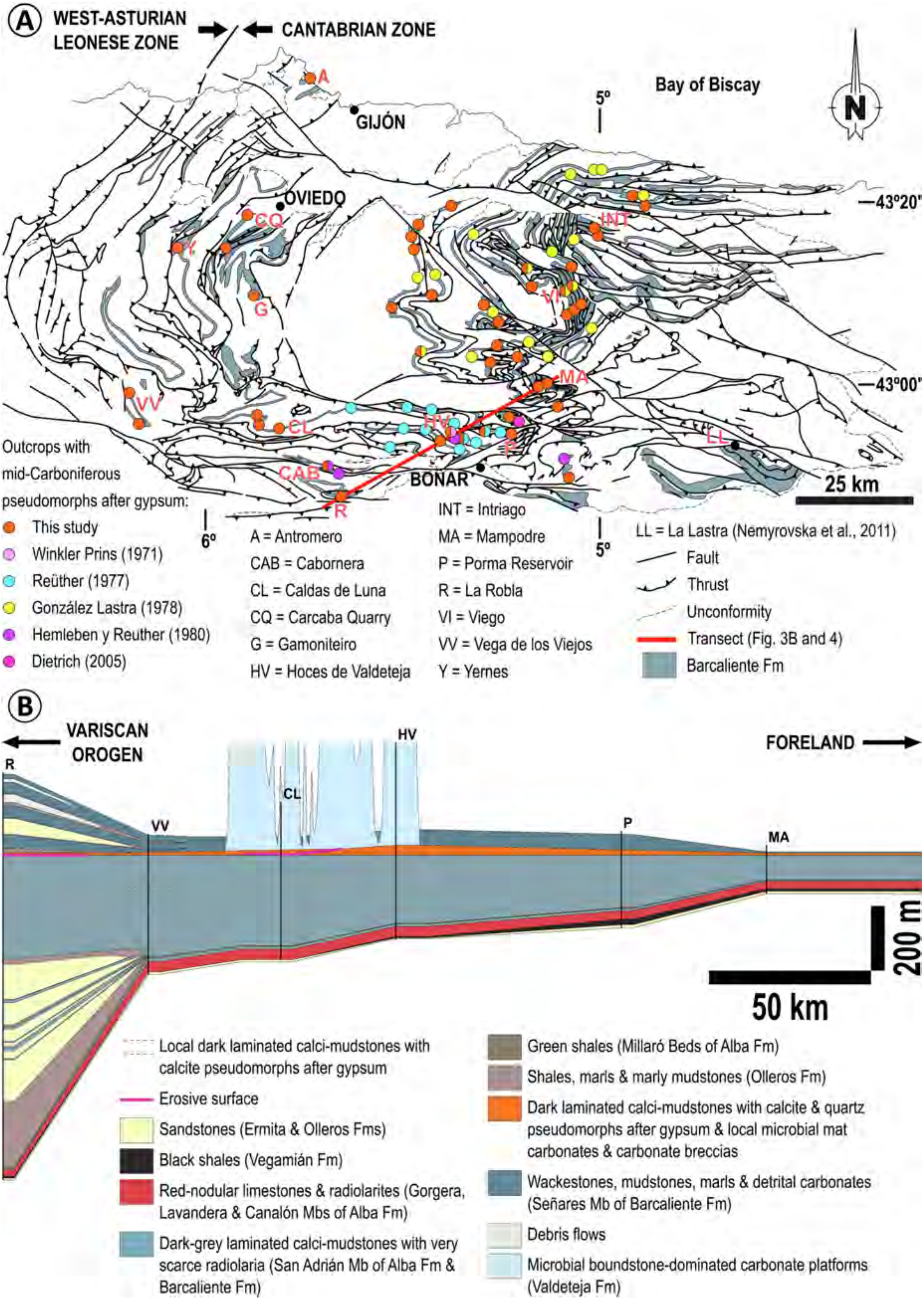
A
WEST-ASTURIAN LEONESE ZONE
CANTABRIAN ZONE
Bay of Biscay
N
5º
GIJÓN
OVIEDO
—43º20"
—43º00"
A
CQ
Y
G
VV
CL
CAB
R
BOÑAR
HV
P
MA
VI
INT
LL
25 km
6º
5º
Outcrops with mid-Carboniferous pseudomorphs after gypsum:
● This study
● Winkler Prins (1971)
● Reüther (1977)
● González Lastra (1978)
● Hemleben y Reuther (1980)
● Dietrich (2005)
A = Antromero
CAB = Cabornera
CL = Caldas de Luna
CQ = Carcaba Quarry
G = Gamoniteiro
HV = Hoces de Valdeteja
INT = Intriago
MA = Mampodre
P = Porma Reservoir
R = La Robla
VI = Viego
VV = Vega de los Viejos
Y = Yernes
LL = La Lastra (Nemyrovska et al., 2011)
Fault
Thrust
Unconformity
Transect (Fig. 3B and 4)
Barcaliente Fm
B
VARISCAN OROGEN
FORELAND
R
VV
CL
HV
P
MA
200 m
50 km
Local dark laminated calci-mudstones with calcite pseudomorphs after gypsum
Erosive surface
Sandstones (Ermita & Olleros Fms)
Black shales (Vegamián Fm)
Red-nodular limestones & radiolarites (Gorgera, Lavandera & Canalón Mbs of Alba Fm)
Dark-grey laminated calci-mudstones with very scarce radiolaria (San Adrián Mb of Alba Fm & Barcaliente Fm)
Green shales (Millaró Beds of Alba Fm)
Shales, marls & marly mudstones (Olleros Fm)
Dark laminated calci-mudstones with calcite & quartz pseudomorphs after gypsum & local microbial mat carbonates & carbonate breccias
Wackestones, mudstones, marls & detrital carbonates (Señares Mb of Barcaliente Fm)
Debris flows
Microbial boundstone-dominated carbonate platforms (Valdeteja Fm)

Figure 3

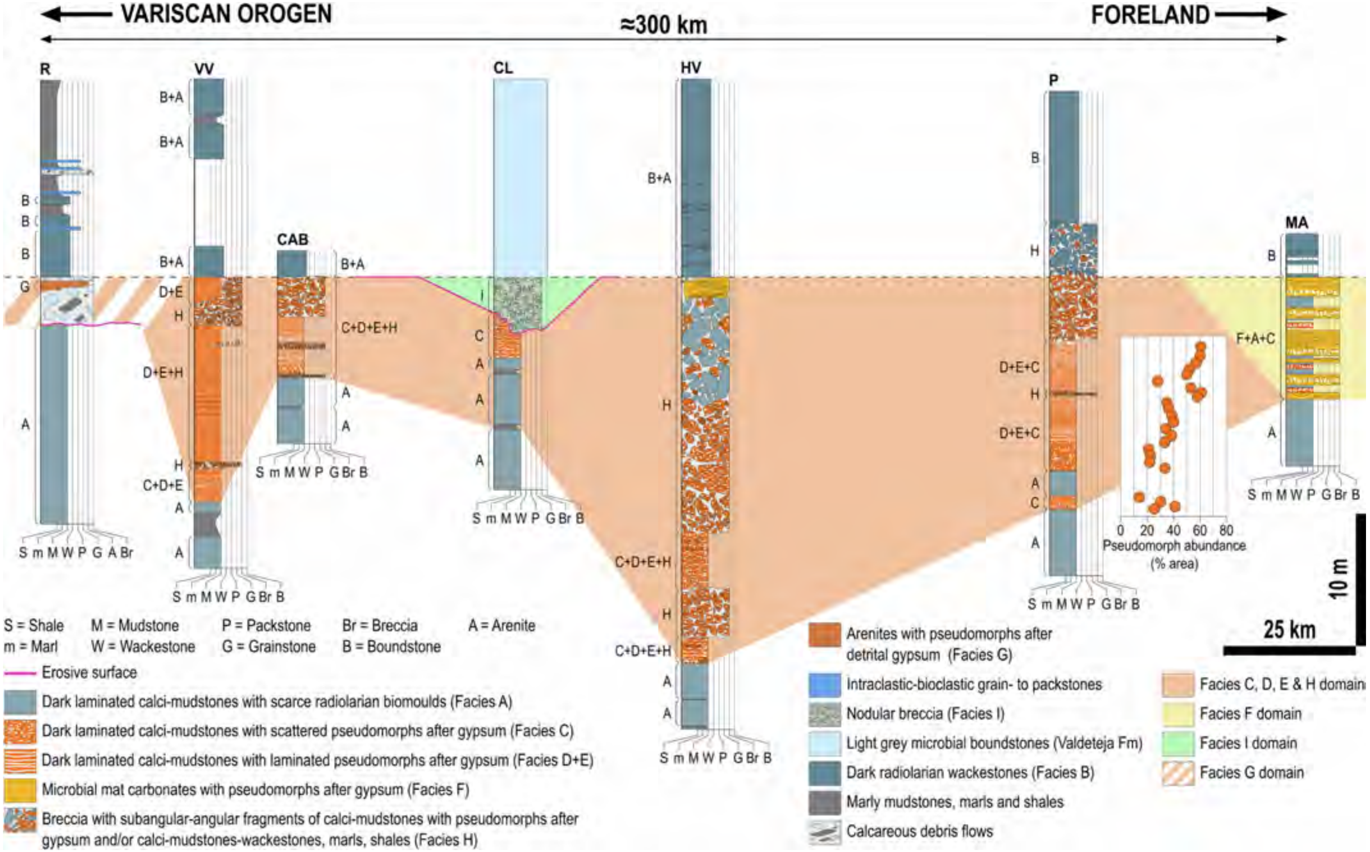
VARISCAN OROGEN
≈300 km
FORELAND
R
VV
CAB
CL
HV
P
MA
B+A
B
G
A
D+E
H
D+E+H
C+D+E
C+D+E+H
I
C
D+E+C
F+A+C
S m M W P G A Br
S m M W P G Br B
0 20 40 60 80
Pseudomorph abundance (% area)
10 m
25 km
S = Shale
m = Marl
M = Mudstone
W = Wackestone
P = Packstone
G = Grainstone
Br = Breccia
B = Boundstone
A = Arenite
Erosive surface
Dark laminated calci-mudstones with scarce radiolarian biomoulds (Facies A)
Dark laminated calci-mudstones with scattered pseudomorphs after gypsum (Facies C)
Dark laminated calci-mudstones with laminated pseudomorphs after gypsum (Facies D+E)
Microbial mat carbonates with pseudomorphs after gypsum (Facies F)
Breccia with subangular-angular fragments of calci-mudstones with pseudomorphs after gypsum and/or calci-mudstones-wackestones, marls, shales (Facies H)
Arenites with pseudomorphs after detrital gypsum (Facies G)
Intraclastic-bioclastic grain- to packstones
Nodular breccia (Facies I)
Light grey microbial boundstones (Valdeteja Fm)
Dark radiolarian wackestones (Facies B)
Marly mudstones, marls and shales
Calcareous debris flows
Facies C, D, E & H domain
Facies F domain
Facies I domain
Facies G domain

Figure 4

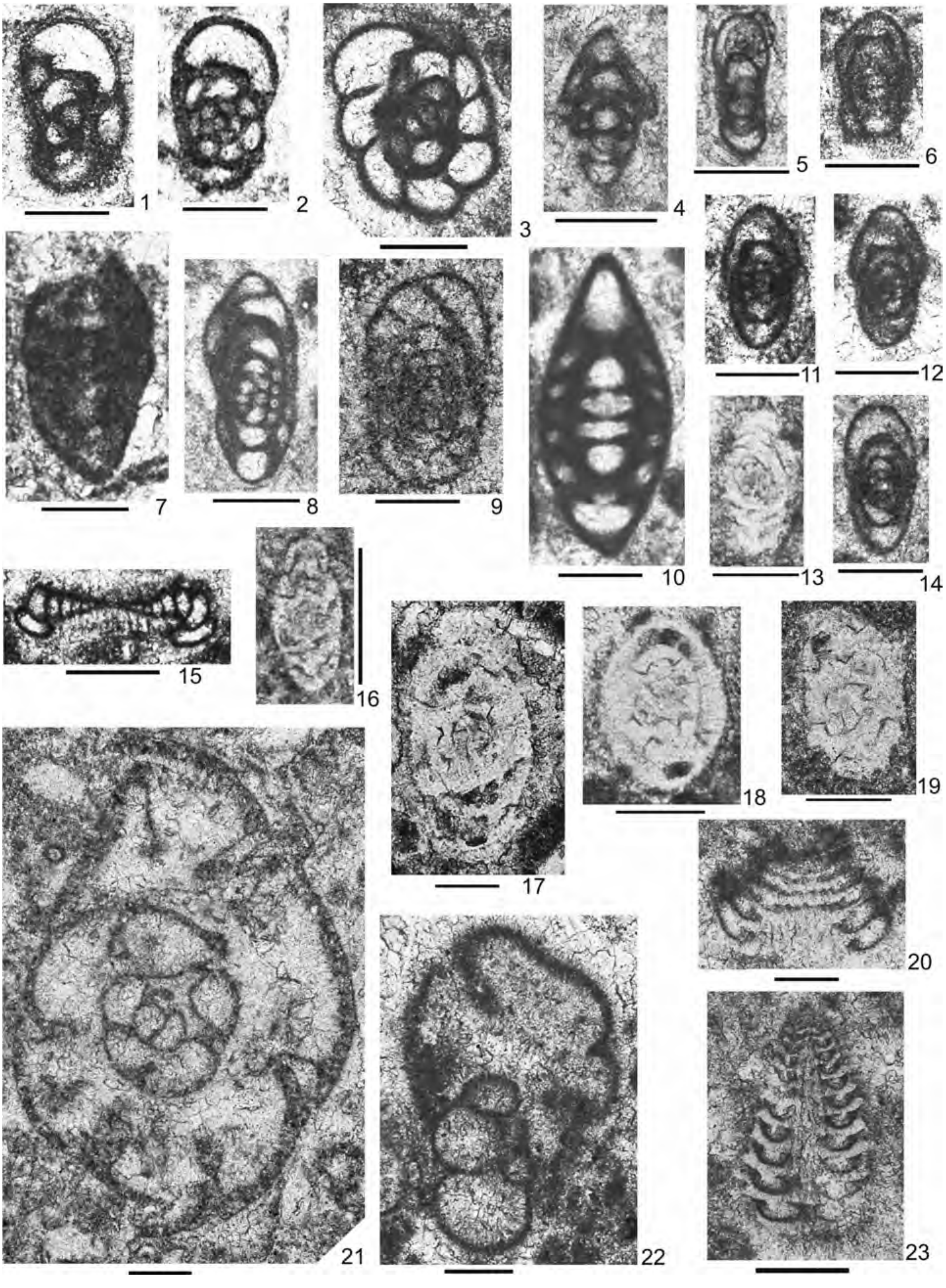

Figure 5

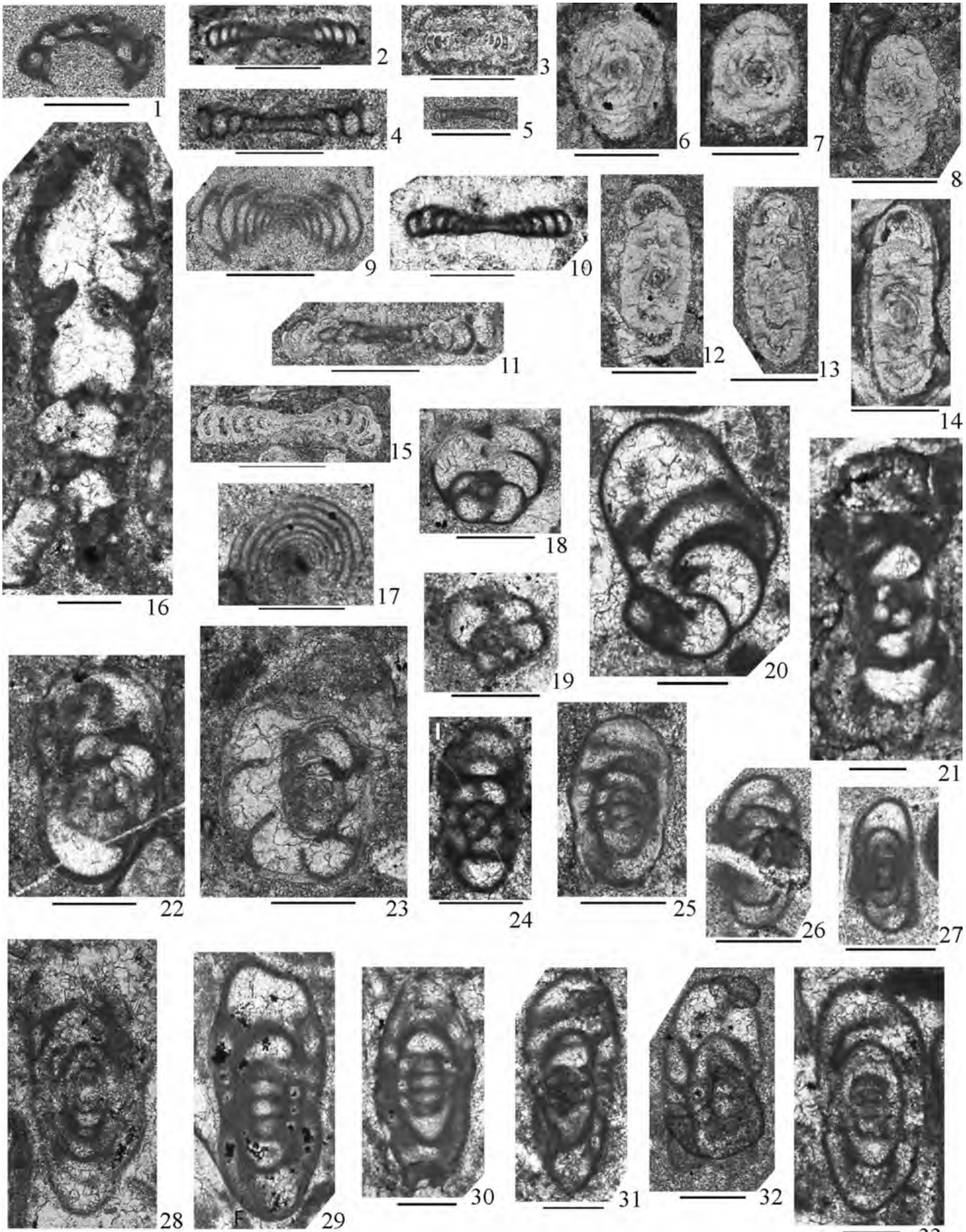
1
2
3
4
5
6
7
8
9
10
11
12
13
14
15
16
17
18
19
20
21
22
23
24
25
26
27
28
29
30
31
32
33

Figure 6

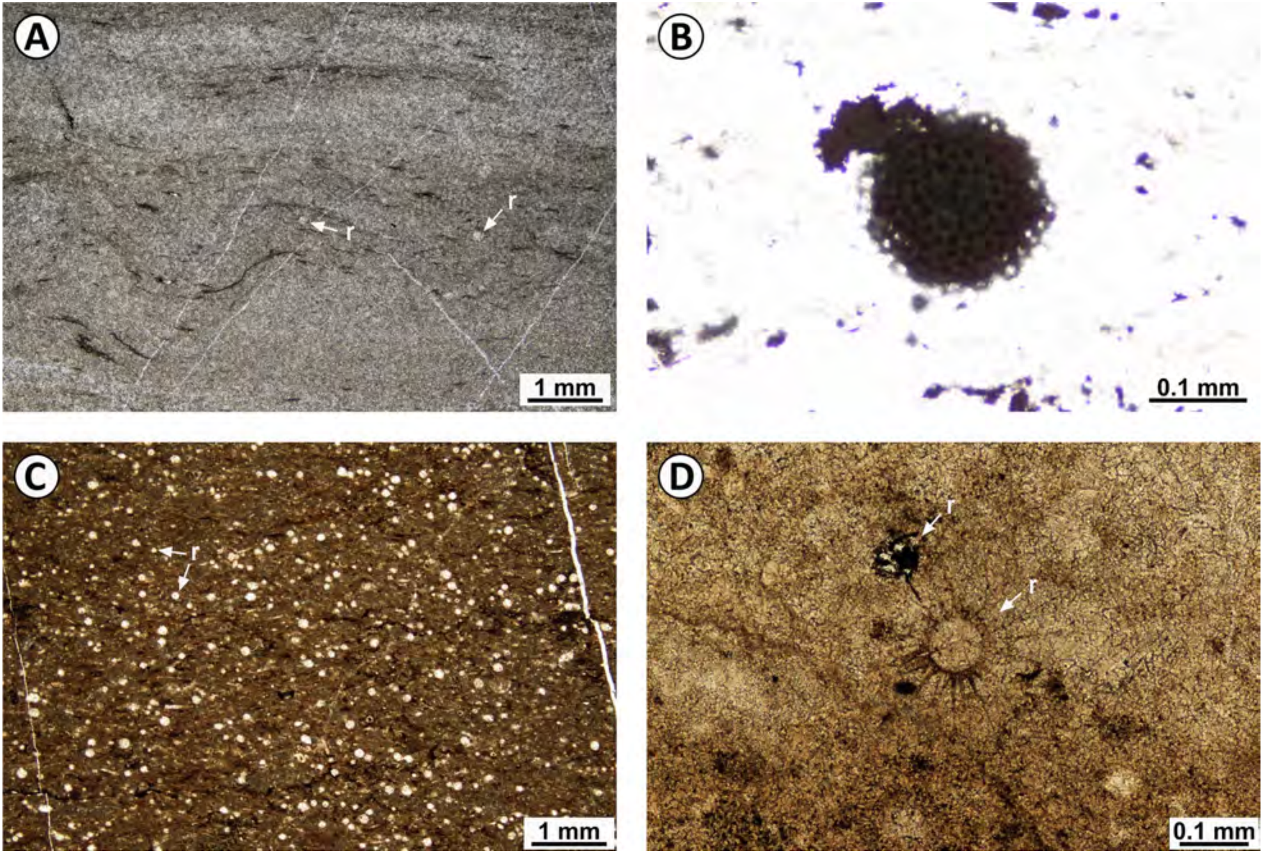

Figure 7

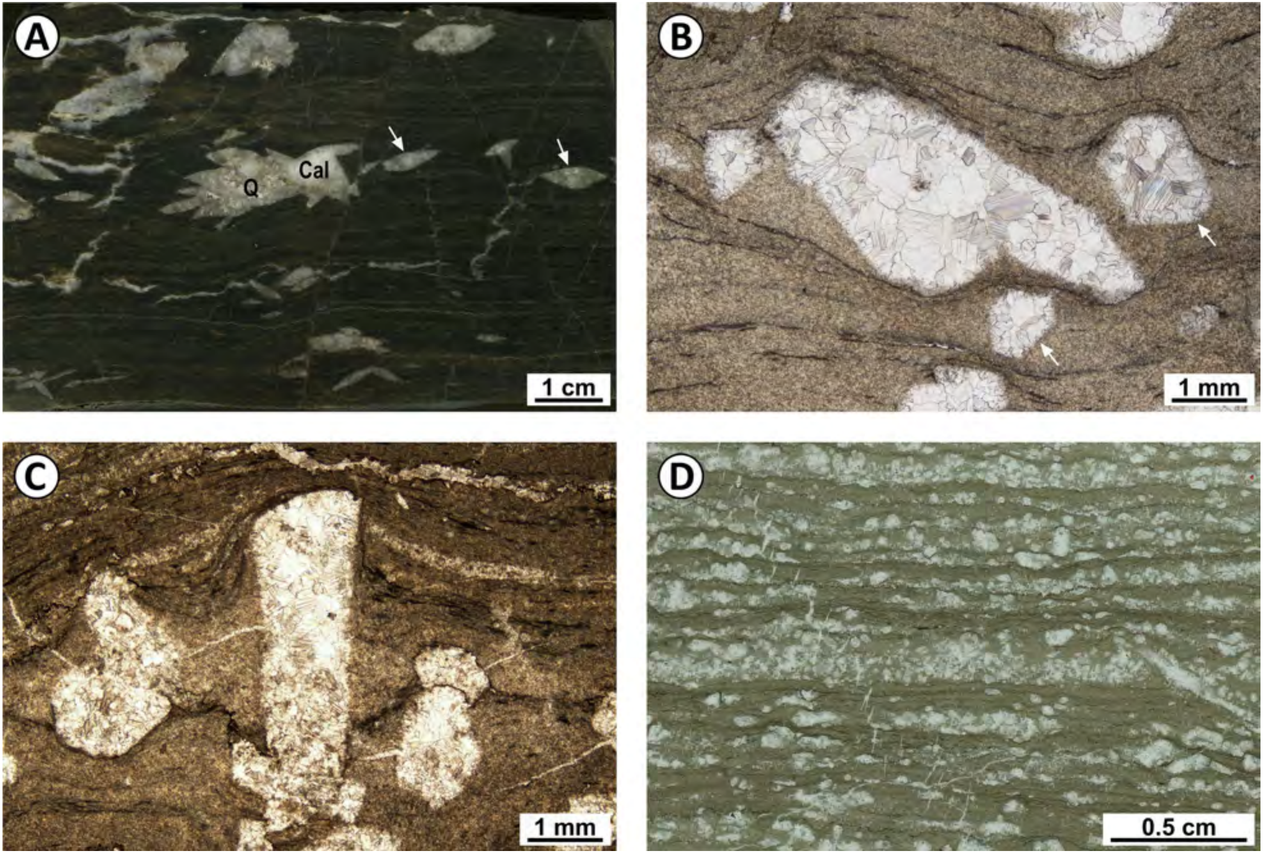

Figure 8

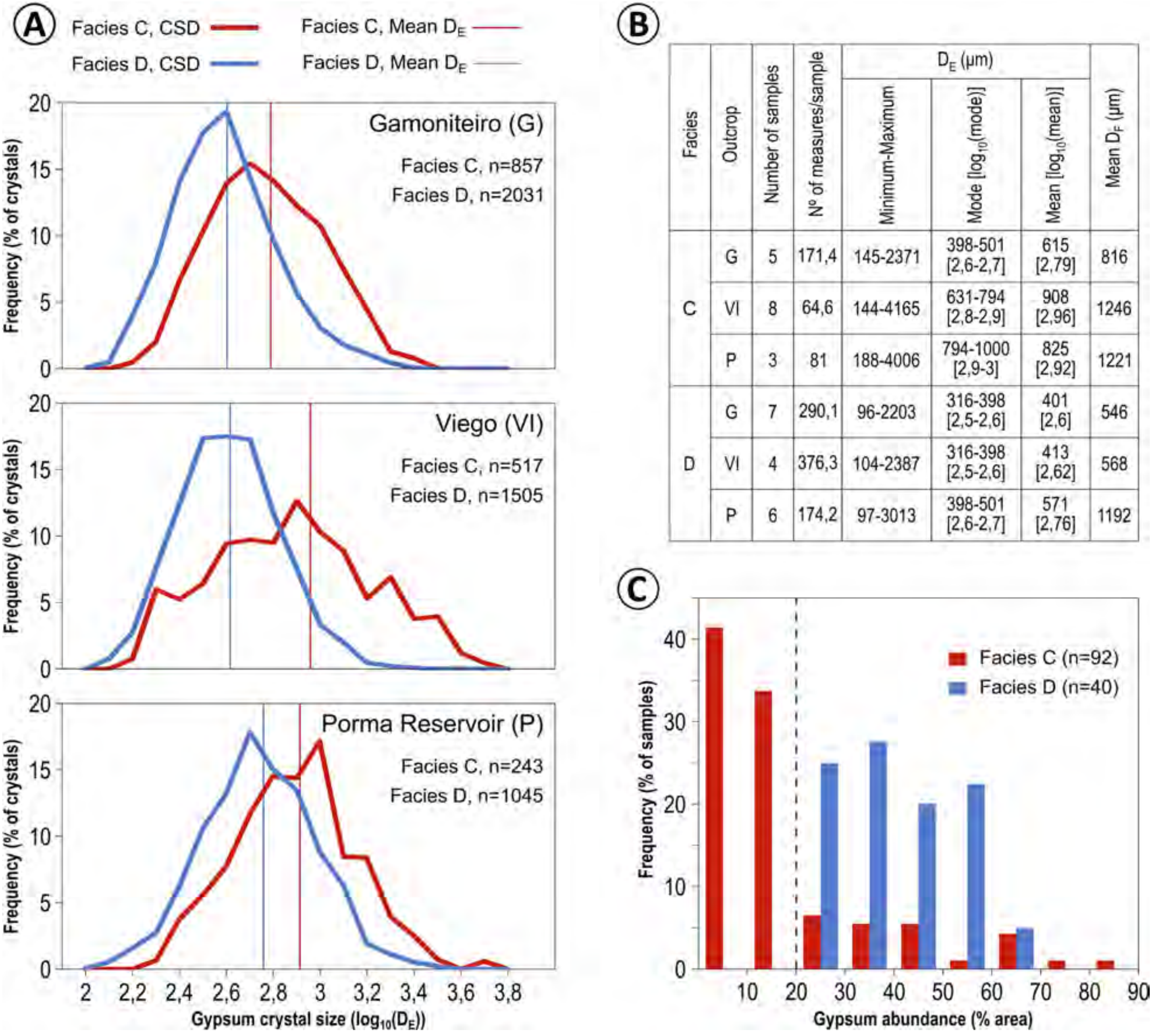

Facies	Outcrop	Number of samples	Nº of measures/sample	D_E (µm) Minimum-Maximum	D_E (µm) Mode [$\log_{10}$(mode)]	D_E (µm) Mean [$\log_{10}$(mean)]	Mean D_F (µm)
C	G	5	171,4	145-2371	398-501 [2,6-2,7]	615 [2,79]	816
	VI	8	64,6	144-4165	631-794 [2,8-2,9]	908 [2,96]	1246
	P	3	81	188-4006	794-1000 [2,9-3]	825 [2,92]	1221
D	G	7	290,1	96-2203	316-398 [2,5-2,6]	401 [2,6]	546
	VI	4	376,3	104-2387	316-398 [2,5-2,6]	413 [2,62]	568
	P	6	174,2	97-3013	398-501 [2,6-2,7]	571 [2,76]	1192

Figure 9

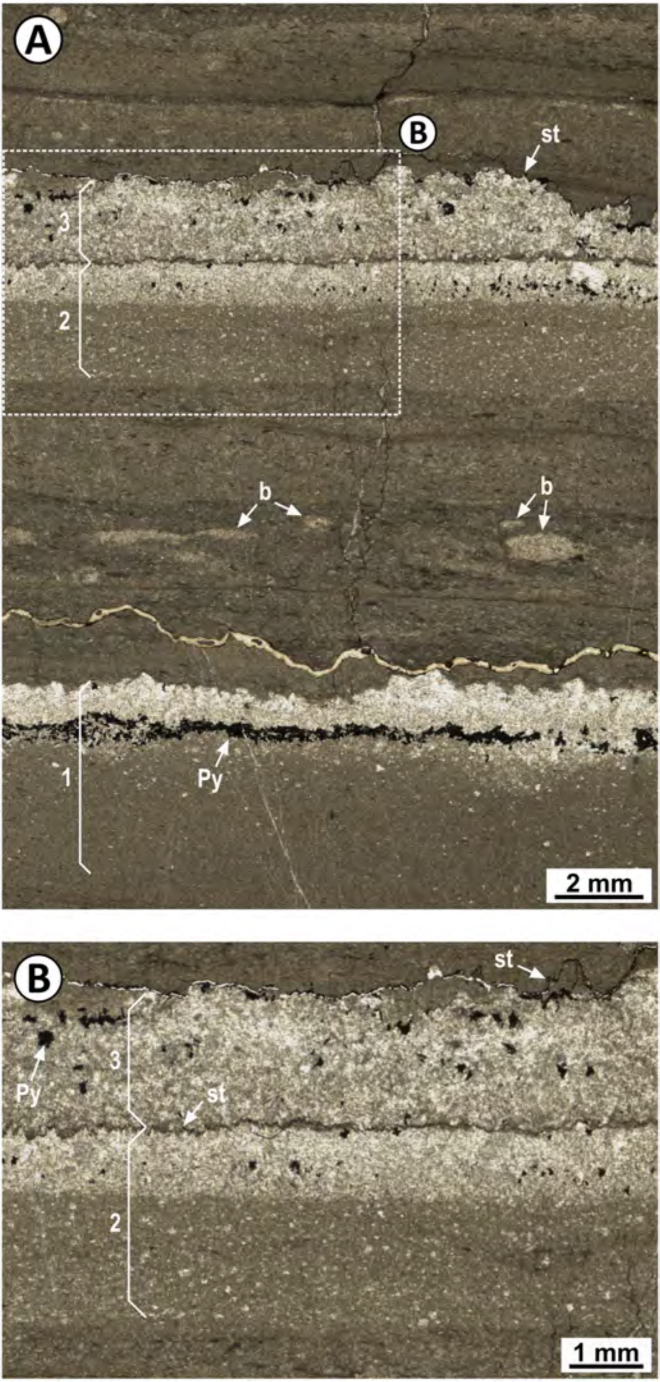

Figure 10

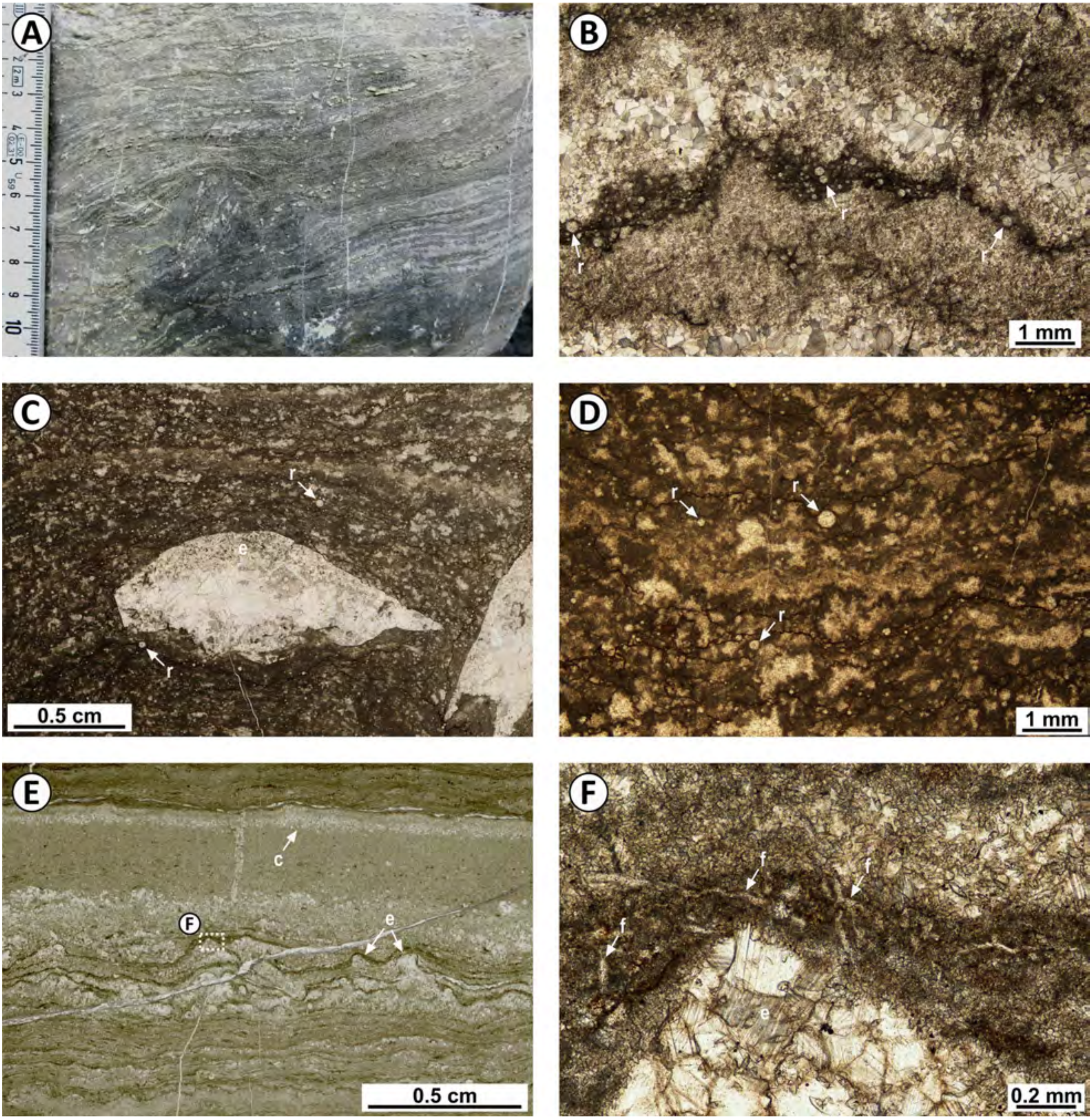

Figure 11

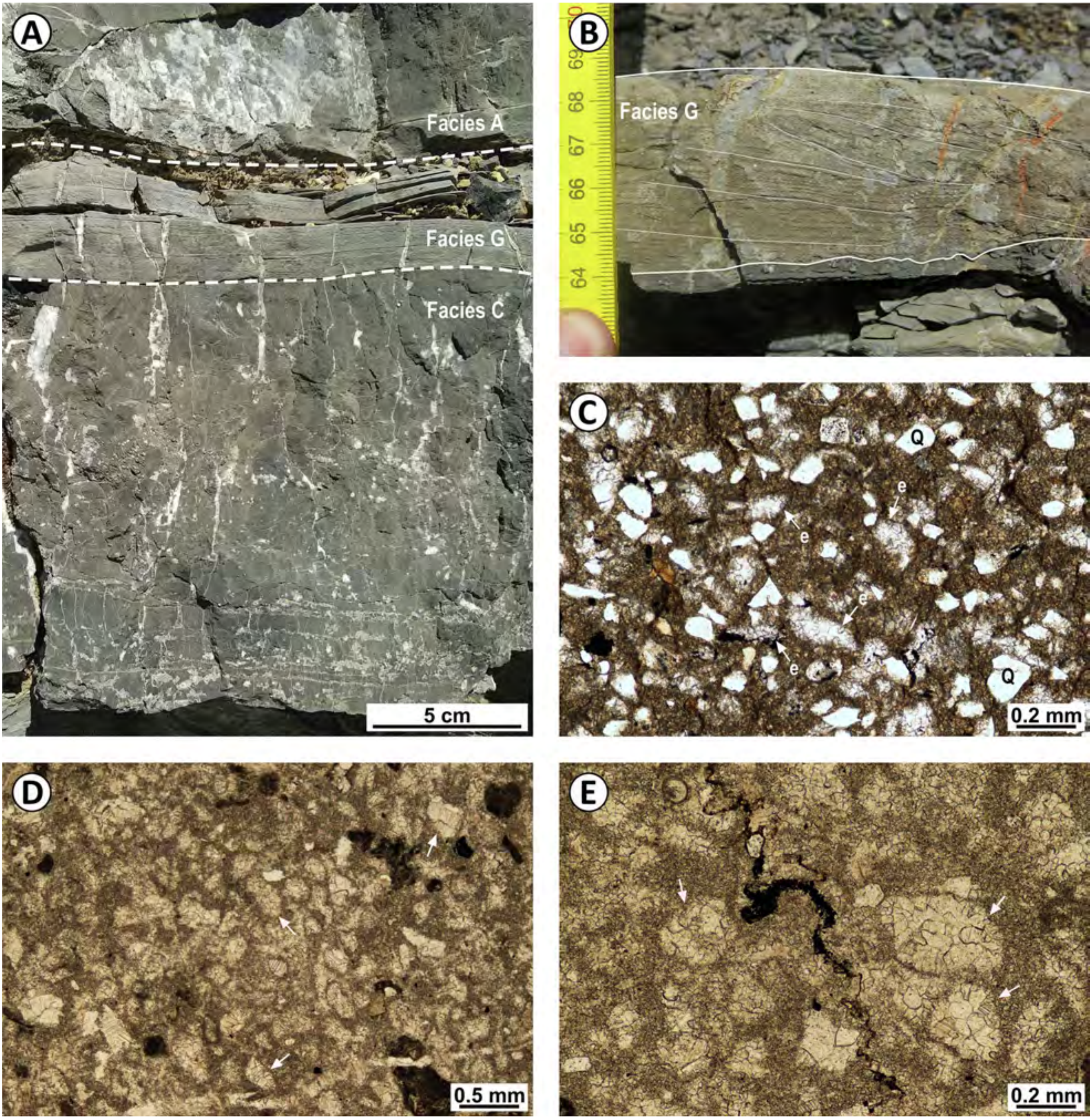
A
Facies A
Facies G
Facies C
5 cm
B
Facies G
64
65
66
67
68
69
C
Q
e
e
e
e
Q
0.2 mm
D
0.5 mm
E
0.2 mm

Figure 12

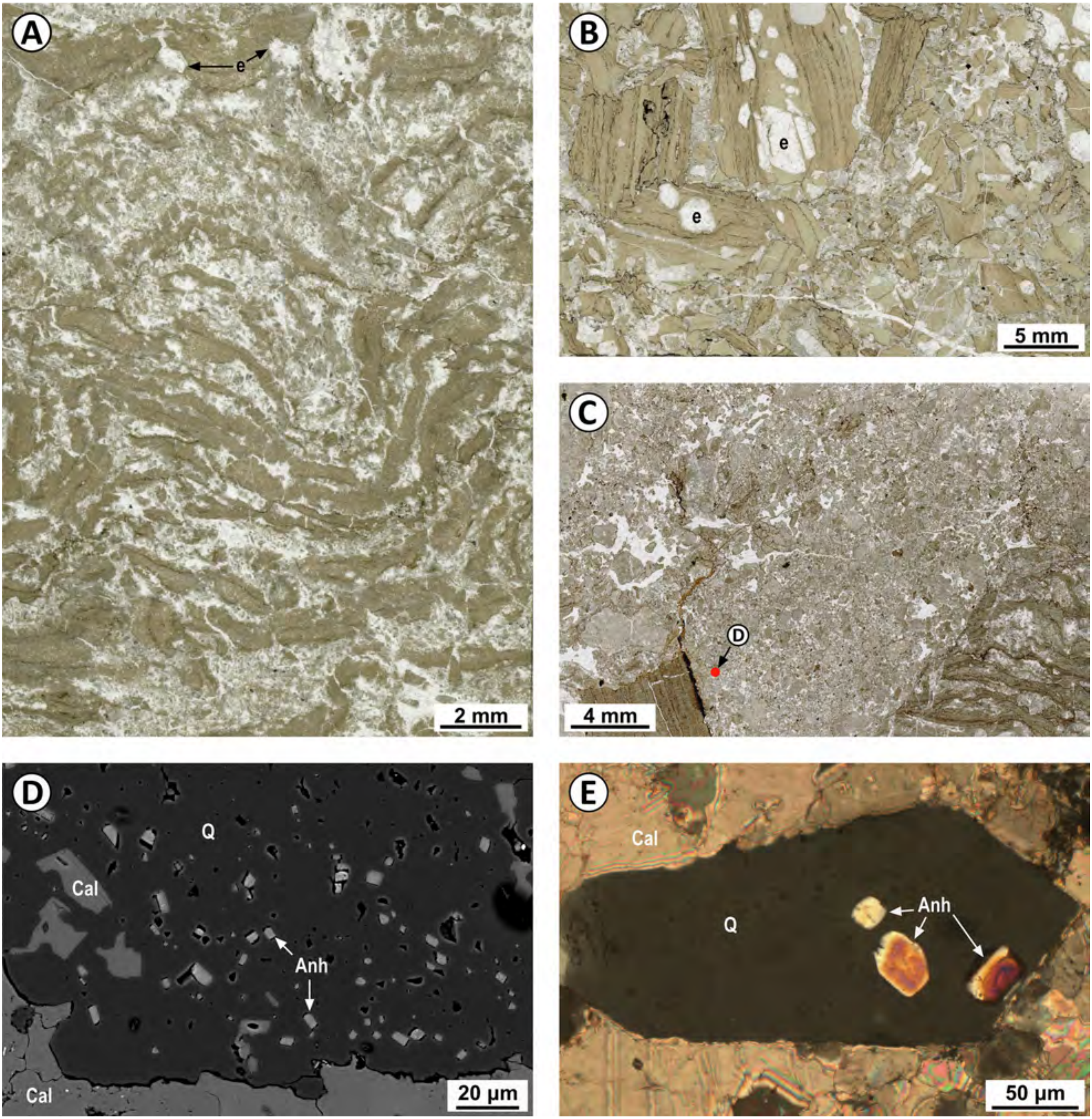

Figure 13

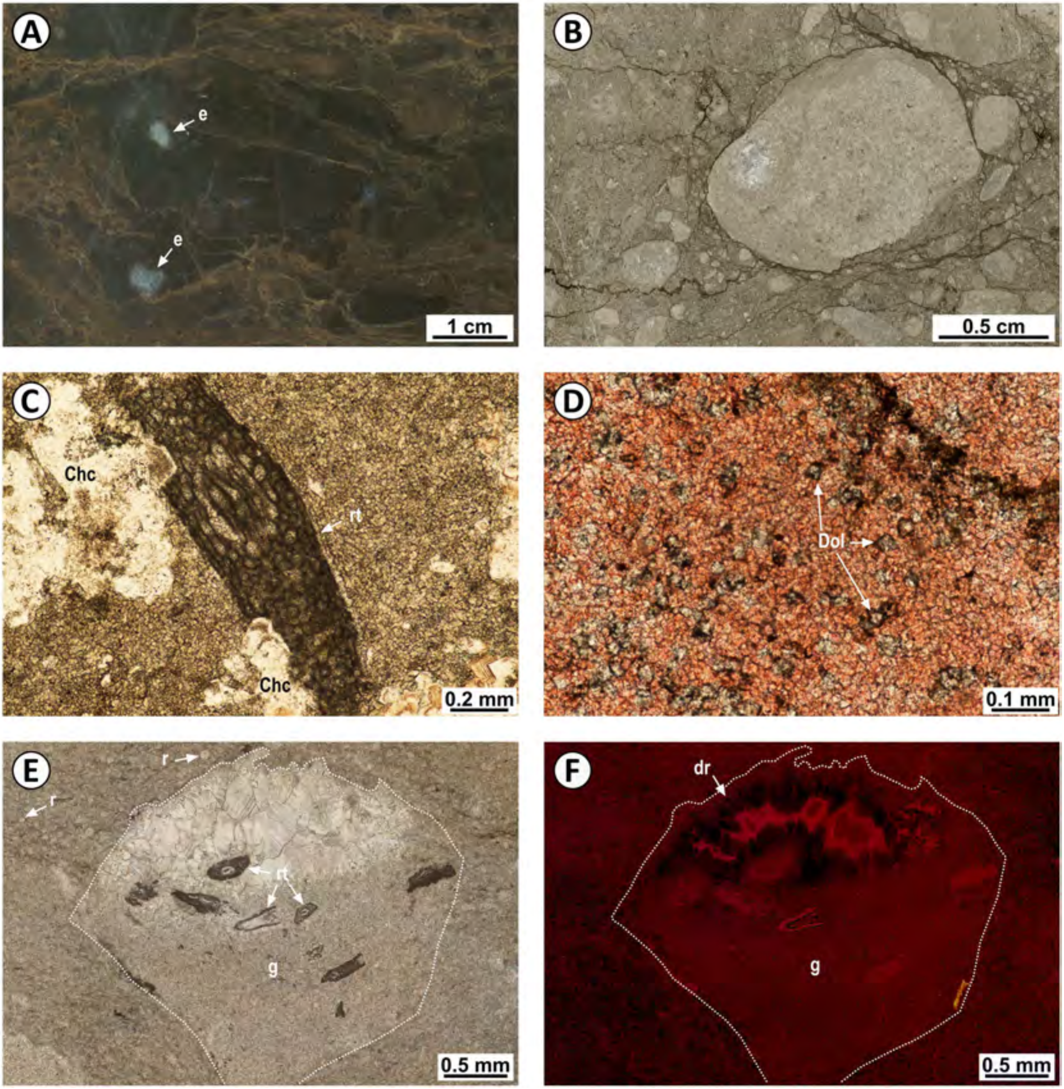
A
e
e
1 cm
B
0.5 cm
C
Chc
rt
Chc
0.2 mm
D
Dol
0.1 mm
E
r
r
rt
g
0.5 mm
F
dr
g
0.5 mm

Figure 14

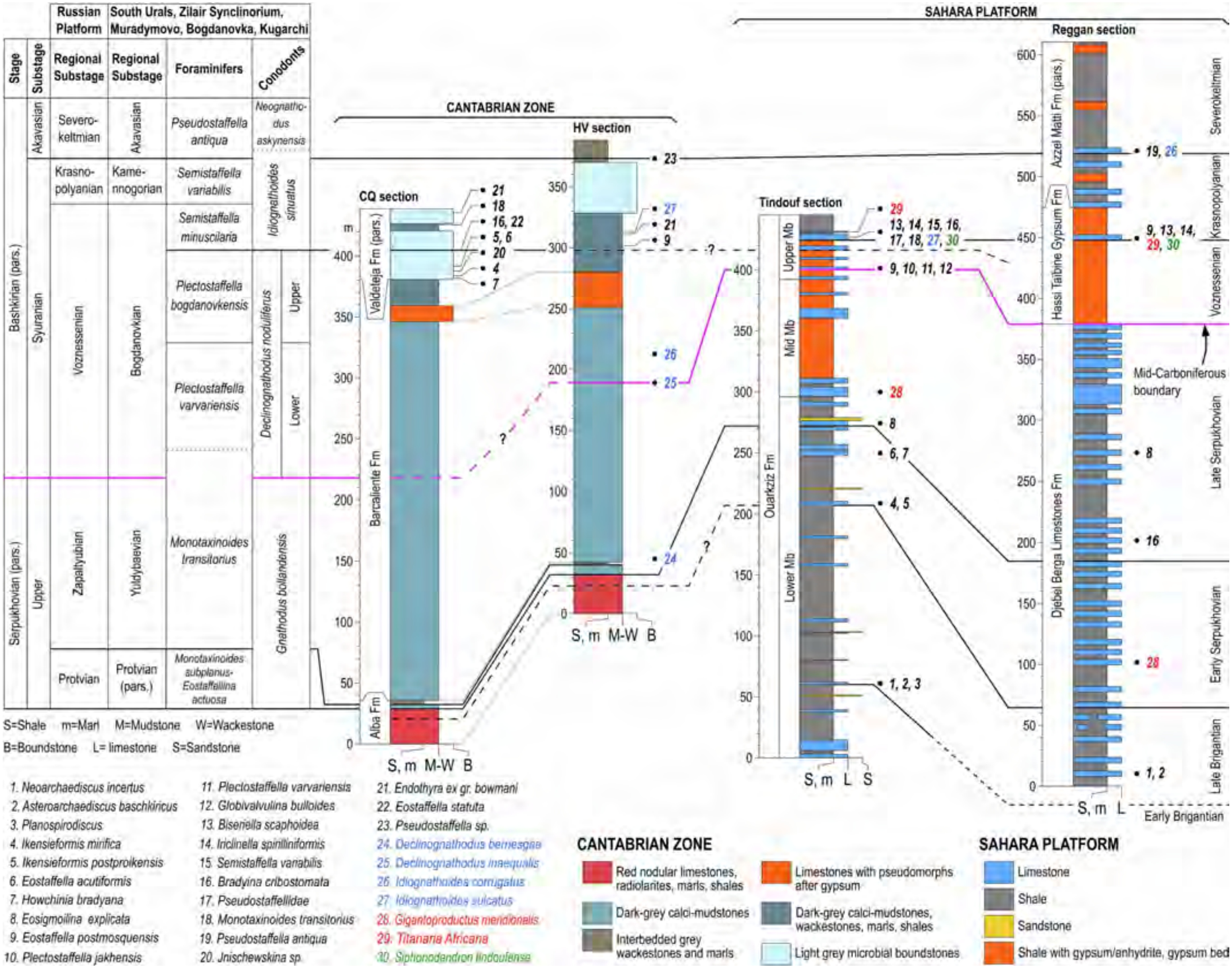
Russian Platform
South Urals, Zilair Synclinorium, Muradymovo, Bogdanovka, Kugarchi
Stage
Substage
Regional Substage
Regional Substage
Foraminifers
Conodonts
Bashkirian (pars.)
Serpukhovian (pars.)
Akavasian
Syuranian
Upper
Severo-keltmian
Krasno-polyanian
Voznessenian
Zapaltyubian
Protvian
Akavasian
Kame-nnogorian
Bogdanovkian
Yuldybaevian
Protvian (pars.)
Pseudostaffella antiqua
Semistaffella variabilis
Semistaffella minuscilaria
Plectostaffella bogdanovkensis
Plectostaffella varvariensis
Monotaxinoides transitorius
Monotaxinoides subplanus-Eostaffellina actuosa
Neognathodus askynensis
Idiognathoides sinuatus
Declinognathodus noduliferus
Upper
Lower
Gnathodus bollandensis
CANTABRIAN ZONE
CQ section
HV section
Valdeteja Fm (pars.)
Barcaliente Fm
Alba Fm
S, m M-W B
SAHARA PLATFORM
Tindouf section
Reggan section
Ouarkziz Fm
Upper Mb
Mid Mb
Lower Mb
S, m L S
Azzel Matti Fm (pars.)
Hassi Taibine Gypsum Fm
Djebel Berga Limestones Fm
S, m L
Severokeltmian
Krasnopolyanian
Voznessenian
Late Serpukhovian
Early Serpukhovian
Late Brigantian
Early Brigantian
Mid-Carboniferous boundary
S=Shale m=Marl M=Mudstone W=Wackestone
B=Boundstone L= limestone S=Sandstone
1. Neoarchaediscus incertus
2. Asteroarchaediscus baschkiricus
3. Planospirodiscus
4. Ikensieformis mirifica
5. Ikensieformis postproikensis
6. Eostaffella acutiformis
7. Howchinia bradyana
8. Eosigmoilina explicata
9. Eostaffella postmosquensis
10. Plectostaffella jakhensis
11. Plectostaffella varvariensis
12. Globivalvulina bulloides
13. Biseriella scaphoidea
14. Iriclinella spirilliniformis
15. Semistaffella variabilis
16. Bradyina cribostomata
17. Pseudostaffellidae
18. Monotaxinoides transitorius
19. Pseudostaffella antiqua
20. Jnischewskina sp.
21. Endothyra ex gr. bowmani
22. Eostaffella statuta
23. Pseudostaffella sp.
24. Declinognathodus bernesgae
25. Declinognathodus inaequalis
26. Idiognathoides corrugatus
27. Idiognathoides sulcatus
28. Gigantoproductus meridionalis
29. Titanaria Africana
30. Siphonodendron tindoufense
CANTABRIAN ZONE
Red nodular limestones, radiolarites, marls, shales
Limestones with pseudomorphs after gypsum
Dark-grey calci-mudstones
Dark-grey calci-mudstones, wackestones, marls, shales
Interbedded grey wackestones and marls
Light grey microbial boundstones
SAHARA PLATFORM
Limestone
Shale
Sandstone
Shale with gypsum/anhydrite, gypsum bed

Figure 15

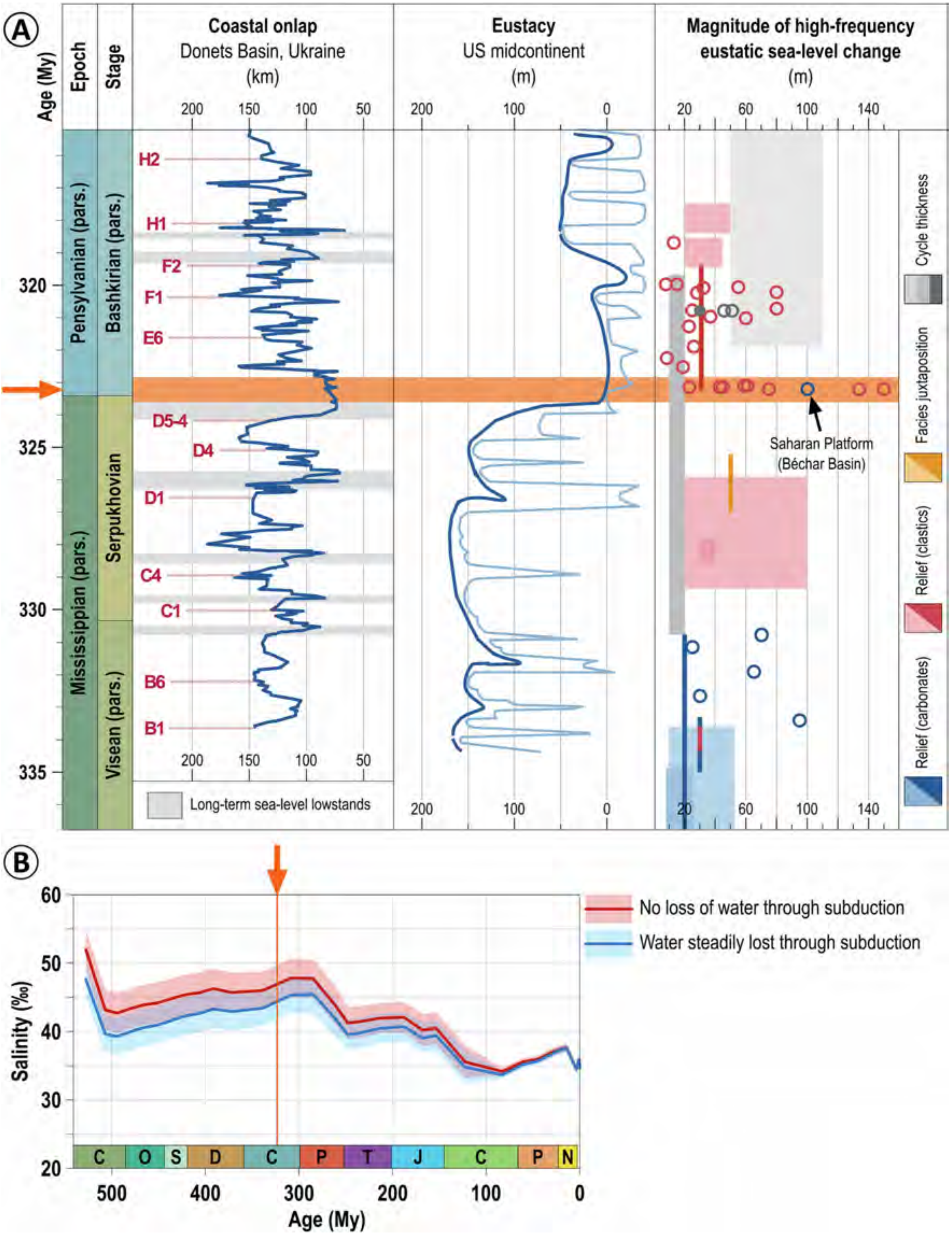
A
Age (My)
Epoch
Stage
Coastal onlap
Donets Basin, Ukraine
(km)
Eustacy
US midcontinent
(m)
Magnitude of high-frequency
eustatic sea-level change
(m)
200
150
100
50
0
20
60
100
140
Pensylvanian (pars.)
Bashkirian (pars.)
Mississippian (pars.)
Serpukhovian
Visean (pars.)
320
325
330
335
H2
H1
F2
F1
E6
D5-4
D4
D1
C4
C1
B6
B1
Long-term sea-level lowstands
Saharan Platform
(Béchar Basin)
Cycle thickness
Facies juxtaposition
Relief (clastics)
Relief (carbonates)
B
Salinity (‰)
60
50
40
30
20
No loss of water through subduction
Water steadily lost through subduction
C
O
S
D
C
P
T
J
C
P
N
500
400
300
200
100
0
Age (My)

Figure 16

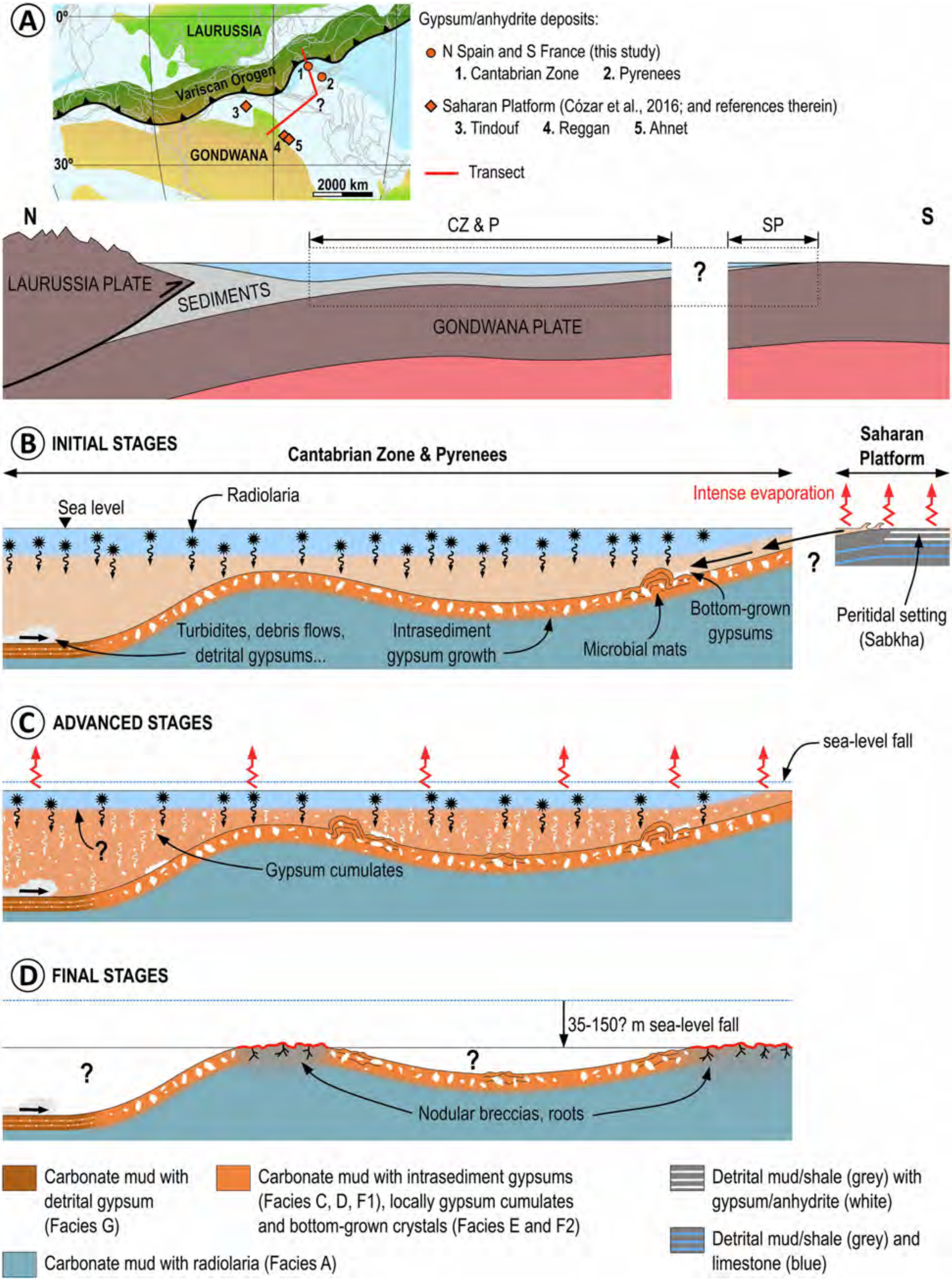
A
0°
30°
LAURUSSIA
Variscan Orogen
GONDWANA
1
2
3
4
5
?
2000 km
Gypsum/anhydrite deposits:
● N Spain and S France (this study)
1. Cantabrian Zone 2. Pyrenees
◆ Saharan Platform (Cózar et al., 2016; and references therein)
3. Tindouf 4. Reggan 5. Ahnet
Transect
N
S
CZ & P
SP
?
LAURUSSIA PLATE
SEDIMENTS
GONDWANA PLATE
B INITIAL STAGES
Cantabrian Zone & Pyrenees
Saharan Platform
Radiolaria
Sea level
Intense evaporation
?
Turbidites, debris flows, detrital gypsums...
Intrasediment gypsum growth
Microbial mats
Bottom-grown gypsums
Peritidal setting (Sabkha)
C ADVANCED STAGES
sea-level fall
?
Gypsum cumulates
D FINAL STAGES
35-150? m sea-level fall
?
?
Nodular breccias, roots
Carbonate mud with detrital gypsum (Facies G)
Carbonate mud with intrasediment gypsums (Facies C, D, F1), locally gypsum cumulates and bottom-grown crystals (Facies E and F2)
Carbonate mud with radiolaria (Facies A)
Detrital mud/shale (grey) with gypsum/anhydrite (white)
Detrital mud/shale (grey) and limestone (blue)

Figure 17